Proteostasis and lysosomal quality control deficits in Alzheimer's disease neurons

Ching-Chieh Chou[1],*, Ryan Vest[4,5,6], Miguel A. Prado[7,8], Joshua Wilson-Grady[7], Joao A. Paulo[7], Yohei Shibuya[9,10], Patricia Moran-Losada[3,5], Ting-Ting Lee[1], Jian Luo[11], Steven P. Gygi[7], Jeffery W. Kelly[12,13], Daniel Finley[7], Marius Wernig[9,10], Tony Wyss-Coray[3,5], Judith Frydman[1,2,3,14]*

[1]Department of Biology, [2]Department of Genetics, Stanford University, Stanford, California, USA

[3]Wu Tsai Neurosciences Institute, Stanford University School of Medicine, Stanford, California, USA

[4]Department of Chemical Engineering, Stanford University, Stanford, California, USA

[5]Department of Neurology and Neurological Sciences, Stanford University, Stanford, California, USA

[6]Qinotto, Inc. San Carlos, California, USA

[7]Department of Cell Biology, Harvard Medical School, Boston, Massachusetts, USA

[8]Instituto de Investigación Sanitaria del Principado de Asturias (ISPA), Oviedo, Spain

[9]Departments of Pathology, Stanford University School of Medicine, Stanford, California, USA

[10]Institute for Stem Cell Biology and Regenerative Medicine, Stanford University School of Medicine, Stanford, California, USA

[11]Palo Alto Veterans Institute for Research, Inc. (PAVIR), Palo Alto, California, USA

[12]Department of Chemistry, The Scripps Research Institute, La Jolla, California, USA.

[13]The Skaggs Institute for Chemical Biology, The Scripps Research Institute, La Jolla, California, USA.

[14]Lead contact

*Corresponding authors: cchou6@stanford.edu (C.-C.C.), jfrydman@stanford.edu (J.F.)

Summary:

The role of proteostasis and organelle homeostasis dysfunction in human aging and Alzheimer's disease (AD) remains unclear. Analyzing proteome-wide changes in human donor fibroblasts and their corresponding transdifferentiated neurons (tNeurons), we find aging and AD synergistically impair multiple proteostasis pathways, most notably lysosomal quality control (LQC). In particular, we show that ESCRT-mediated lysosomal repair defects are associated with both sporadic and PSEN1 familial AD. Aging- and AD-linked defects are detected in fibroblasts but highly exacerbated in tNeurons, leading to enhanced neuronal vulnerability, unrepaired lysosomal damage, inflammatory factor secretion and cytotoxicity. Surprisingly, tNeurons from aged and AD donors spontaneously develop amyloid-β inclusions co-localizing with LQC markers, LAMP1/2-positive lysosomes and proteostasis factors; we observe similar inclusions in brain tissue from AD patients and APP-transgenic mice. Importantly, compounds enhancing lysosomal function broadly ameliorate these AD-associated pathologies. Our findings establish cell-autonomous LQC dysfunction in neurons as a central vulnerability in aging and AD pathogenesis.

Keywords:

Lysosome, Proteostasis, Transdifferentiated neuron, Aging, Alzheimer's disease, Proteomics

INTRODUCTION

Aging is the most prominent risk factor for AD(Alzheimer's Association, 2020; Harvey et al., 2003; Qiu et al., 2009). Most cases are sporadic AD (sAD) and manifest late-onset symptoms. In contrast, less than 5% of cases arise from familial AD (fAD) caused by pathogenic mutations in causative genes with age of onset before 65 years.

The molecular bases of AD dysfunction are poorly understood. Given that accumulation of amyloid plaques and neurofibrillary tangles in the brain are hallmarks of AD(DeTure and Dickson, 2019), it has been proposed that loss of proteostasis is a central contributing factor. AD has also been linked to collapse of mitochondrial and endoplasmic reticulum homeostasis(Chakravorty et al., 2019; Nijholt et al., 2011), and autophagic pathology, including the presence of dystrophic neurites with accumulations of lysosomes, in the brain of AD patients(Gowrishankar et al., 2015; Nixon and Yang, 2011; Piras et al., 2016). Another less-studied AD hallmark, granulovacuolar degeneration (GVD), is characterized by the presence of membrane-bound vacuoles immuno-positive for endocytic vesicle and lysosome markers, such as CHMP2B and LAMP1/2. The formation of GVD bodies is selective to pyramidal neurons and associated with the early stages of amyloid-β (Aβ) and tau pathology in AD(Riku et al., 2019; Su et al., 2002; Wiersma et al., 2019; Yamoah et al., 2020). Taken together, these lines of evidence implicate defective proteostasis and/or organelle homeostasis as early pathogenic events preceding overt neuronal loss in AD. However, whether and how proteostasis and organelle homeostasis defects are directly linked to human aging and AD, and if so, whether they occur in aged or AD neurons in a cell autonomous manner, remains unclear.

68 The maintenance of proteostasis requires many chaperones and protein quality control systems
69 that uphold the delicate balance between protein synthesis, folding and degradation(Hipp et al.,
70 2014). Additionally, the proteostasis network is critically required for the biogenesis, repair and
71 quality control of cellular organelles(Douglas and Dillin, 2010; Galluzzi et al., 2017; Kaushik and
72 Cuervo, 2015). The inter-relationship between protein and organelle quality control is
73 highlighted by the role of soluble proteostasis factors such as Hsp70 and the ubiquitin-
74 proteasome pathway in organelle quality control(Craig, 2018; Pohl and Dikic, 2019) as well as
75 the role of organelle functions, such as lysosomal degradation or mitochondrial energy
76 production, in proteostasis maintenance(Anding and Baehrecke, 2017; Gottschling and
77 Nyström, 2017). The inter-relatedness of these pathways likely renders cellular health
78 vulnerable to extensive dysfunction of a given proteostasis pathway or organelle, which would
79 predispose cells to damage accumulation over time.

80

81 While model systems have offered insights into the link between aging, amyloid disease and
82 disruption of proteostasis or organelle function (Cuervo and Wong, 2014; Douglas and Dillin,
83 2010; Hughes and Gottschling, 2012; Labbadia and Morimoto, 2015), studying the cell biology
84 of aging and AD in human systems has been extremely challenging. Since induced pluripotent
85 stem (iPS) cell reprogramming rejuvenates the epigenome, transcriptome and
86 proteome(Hansson et al., 2012; Mertens et al., 2015; Miller et al., 2013; Studer et al., 2015),
87 neurodegeneration models using embryonic stem cells or iPS cells to generate induced
88 neuronal systems (iNs) forgo the key contribution of aging to AD phenotypes. In contrast, direct
89 transdifferentiation of human adult somatic cells into neurons (herein tNeurons since iNs is also
90 used to refer to iPS cell-derived neurons) enables the preservation of aging signatures in
91 cellular models(Huh et al., 2016; Kim et al., 2018b; Mertens et al., 2015; Pang et al., 2011;
92 Vierbuchen et al., 2010). In recent years, specific tNeuron subtypes have been generated by

93 independent laboratories for modeling neurodegenerative diseases(Caiazzo et al., 2011;
94 Mertens et al., 2021; Tang et al., 2017; Victor et al., 2018). tNeurons with characteristics of
95 cortical neurons derived from AD patients were shown to recapitulate sAD-related alterations in
96 transcriptome and metabolome(Mertens et al., 2021; Traxler et al., 2022). Hence, we
97 hypothesized that tNeurons are amenable to define how aging and AD change the proteome.

98

99 We here undertook the proteomic and cell biological characterization of proteostasis and
100 organelle homeostasis changes in AD. We obtained human adult fibroblasts from young, aged
101 and AD donors and used them to generate tNeurons. We then assessed how aging and AD
102 change the cellular proteome of fibroblasts and their derived tNeurons (Figure 1A). Cellular and
103 molecular characterization of neuronal phenotypes were extended and supported by histological
104 validation in post-mortem mouse and human brain tissue. Strikingly, we found that aging and
105 AD lead to substantial alterations in the proteomes and cell biological functions of both patient-
106 derived fibroblasts and tNeurons. Quantitative proteomics analysis indicated deficits in
107 proteostasis and organelle homeostasis, with dramatic changes in the endosome-lysosome
108 pathway. Our findings indicate aging and AD act synergistically to impair proteostasis and
109 lysosomal homeostasis. Notably, tNeurons were significantly more vulnerable than fibroblasts to
110 deficits in lysosomal repair and recovery from damage. Thus, AD tNeurons contained
111 constitutively damaged lysosomes, as well as Aβ and hyper-phosphorylated tau (pTau)
112 deposits; they also secreted pro-inflammatory factors and were susceptible to neuronal death.
113 Highlighting the centrality of lysosomal function to AD-linked phenotypes, pharmacological
114 rescue of damaged lysosomes in both fibroblasts and tNeurons alleviated cell-based aging and
115 AD pathologies. We conclude that human tNeurons provide a model for assessing cell-
116 autonomous aging and AD phenotypes and a powerful platform to explore the cell biology and
117 therapeutic targets of AD.

118 **RESULTS**

119 **Proteostasis deficits in human fibroblasts derived from aged and AD donors**

120 To develop cellular models for aging and AD, we collected fibroblasts from healthy young (age
121 27.2 ± 4.0) and aged donors (age 71.1 ± 5.5), as well as aged patients with sAD (herein
122 aged/sAD, age 67.7 ± 6.9) and fAD patients with PSEN1 mutations (herein fAD-PSEN1, age
123 41.3 ± 9.0) (Table S1). We observed a correlation of donor's age and disease status with age-
124 and disease-associated markers, including those previously described in AD brain
125 tissue(Mansuroglu et al., 2016; Nativio et al., 2018; Salminen et al., 2012). Compared with
126 fibroblasts of young donors, fibroblasts from aged and aged/sAD donors showed an increase in
127 DNA damage measured by γ-H2AX puncta (Figure 1B) and a global loss of epigenetic marker,
128 histone 3 lysine 9 trimethylation (H3K9me3) (Figure 1C). Histone H4 lysine 16 acetylation
129 (H4K16ac) became enriched during aging but reduced with AD (Figure 1C). This recapitulated
130 findings in a genome-wide assessment of histone modifications of the human brain, which
131 observed H4K16ac enriched in normal aging but reduced in AD(Nativio et al., 2018).

132

133 To assess if human fibroblasts exhibit aging- and AD-linked proteostasis defects, we examined
134 the accumulation of ubiquitin-positive puncta as well as autophagy receptor p62/SQSTM1. No
135 inclusions were observed under basal conditions, but the treatment with proteasome inhibitor
136 Bortezomib (BTZ) or autophagy inhibitor Chloroquine (CQ) led to a moderate increase in the
137 accumulation of ubiquitin and p62/SQSTM1 puncta in aged fibroblasts (Figures 1D and 1E).
138 Strikingly, the protein accumulations were significantly exacerbated in aged/sAD fibroblasts,
139 suggesting that proteostasis dysfunction and susceptibility to proteotoxic stress is more acute in
140 aged/AD cells than in normal aged cells.

141

142 **Human fibroblasts reveal proteome-wide changes related to aging and AD**

143 To understand how aging and sAD affect the proteome of primary human fibroblasts, we carried
144 out a global quantification of proteins in our donor set via multiplex Tandem Mass Tag (TMT)
145 labeling. A total of 7,314 proteins were quantified from each sample. The proteins with fewer
146 than two unique peptides were excluded, resulting in 5,747 proteins used for further analysis.
147 Hierarchical and differential expression analysis identified changes in relative protein
148 abundance across samples (Figures S1A and S1B) and top proteomic hits (Figure S1C). These
149 analyses revealed aging and sAD impact proteostasis. Top-ranked pathways impacted by aging
150 and sAD revealed by gene ontology (GO) (Figure S1D) and integrated network analysis
151 (Figures 1F and S1E), corresponded to endosome-lysosome function and repair, protein folding,
152 inflammation, and cytoskeleton remodeling. In proteome of aging fibroblasts, we observed the
153 up-regulation of endosome-lysosomal proteins targeted to endosomal-sorting complex (e.g.
154 CHMP6 and RAB43) and lysosomal degradation (e.g. CTSB and CTSL), and down-regulation of
155 proteins for forming the ferritin complex (e.g. FTL and FTH1) (Figure 1F and 1G). In the
156 proteome of aging/sAD fibroblasts, endosome-lysosomal proteins were down-regulated,
157 particularly those involved in the molecular machinery for regulating lysosomal pH (e.g. v-
158 ATPases: ATP6V0D1 and ATP6AP1). In addition, the aging/sAD proteome exhibited significant
159 changes in mitochondrial proteins (Fig. 1F). To better understand the divergent trajectories in
160 proteome changes in aging versus aging/sAD, we performed a cluster analysis based on the
161 similarity of protein expression across young, aged and aged/sAD fibroblasts (Figure 1H). The
162 similarity matrix identified three main cluster trajectories in proteostasis pathways changing
163 during healthy aging versus aging/sAD, which impacted most lysosomal proteolysis pathways
164 and subsets of protein folding and chaperone factors, as well as translation machinery
165 components. These data indicate that aging changes the cellular proteome to alter proteostasis
166 and organelle homeostasis pathways. Notably, aging with sAD exacerbates these proteome

167 changes. These findings are consistent with the progressive increase in vulnerability observed
168 from aged to aged/sAD fibroblasts to proteotoxic stress.

169

170 **Enhanced proteostasis deficits in human tNeurons are linked to aging and AD protein**
171 **pathologies**

172 We next transdifferentiated the primary fibroblasts from young, aged, aged/sAD and fAD-
173 PSEN1 donors characterized above into neurons. Introducing transcription factors Brn2, Ascl1,
174 Myt1l, and Ngn2 (herein BAMN factors) yielded a majority of tNeurons with cortical neuron
175 characteristics (Figures 2A and S2B and & Table S1), as previous studies reported(Pang et al.,
176 2011; Tanabe et al., 2018). At post-induction day (PID) 35 to 42, tNeurons expressed neuronal
177 markers Tuj1, MAP2, NeuN, Tau, GAP43 and Synapsin-1 (Syn-1) (Figures 2A and S2C). The
178 aged and aged/sAD donors showed a slight reduction in fibroblast-to-neuron reprogramming
179 efficiency and synaptic density identified by Syn-1 puncta (Figures 2A and S2C). Direct
180 conversion to tNeurons retained aging hallmarks, since aged/sAD tNeurons also exhibited the
181 age-related increase in DNA damage (Figure 2B), global loss of H3K9me3 and H4K16ac
182 redistribution (Figure 2C) observed in the donor's fibroblasts. We next examined whether
183 tNeurons exhibit aging- and AD-linked proteostasis deficits. Notably, even under basal
184 conditions, the tNeurons derived from aged and AD donors contained p62/SQSTM1 and
185 ubiquitin puncta (Figures 2D and S2D). This contrasted to their corresponding fibroblasts, where
186 these proteostasis deficits were only uncovered upon BTZ or CQ treatment (Figures 1D and
187 1E). Further, we observed significantly more p62/SQSTM1 puncta in both aged/sAD and fAD-
188 PSEN1 tNeurons than in aged tNeurons.

189

190 The above analyses suggest neuronal proteostasis is more vulnerable to aging and AD than
191 that of the parental fibroblasts. This led us to examine formation of AD-associated protein
192 pathologies in tNeurons (Figures 2D and S2D). Remarkably, aging tNeurons contained a higher
193 burden of intracellular total Aβ, the toxic isoform Aβ42, pTau, hyper-phosphorylated TDP-43
194 (pTDP-43) in tNeurons (Figures 2D and S2D). Strikingly, these pathological protein deposits
195 were significantly increased in tNeurons from aged/sAD donors (Figures 2D and S2D). The
196 clear progressive enrichment in these AD phenotypes between aged and aged/AD tNeurons,
197 suggests a cooperative contribution of aging to sAD dysfunction. The strongest enrichment in
198 protein pathology was observed in fAD-PSEN1 tNeurons, suggesting that genetic mutations can
199 have a great impact on neuronal proteostasis. Of note, TDP-43 pathology is the hallmark of
200 amyotrophic lateral sclerosis (ALS) and frontotemporal dementia (FTD)(Chou et al., 2018). The
201 increase in pTDP-43 and loss of nuclear TDP-43 in aged, aged/sAD and fAD-PSEN1 tNeurons
202 (Figures 2D and S2D) resonates with findings that TDP-43 pathology concurrence in 23-50% of
203 AD as a potential co-factor (Amador-Ortiz et al., 2007; Josephs et al., 2014) and suggests that a
204 cell-intrinsic deficit in proteostasis can lead to multiple protein pathologies. These experiments
205 uncover the increased fragility of neuronal proteostasis to aging and AD as compared to
206 fibroblasts and establish that aging and AD cooperatively promote cell-intrinsic accumulations of
207 multiple AD-linked protein pathologies, including Aβ, pTau and pTDP-43.

208

209 **Quantitative proteomics uncovers how aging and AD alter the neuronal proteome**

210 While transcriptomic changes in aged and AD derived neurons have been extensively
211 characterized(Grubman et al., 2019; Mathys et al., 2019; Raj et al., 2018), how these conditions
212 affect the proteome of patient-derived neurons has not been examined. We carried out
213 quantitative analyses of proteome changes in young, aged and AD-derived tNeurons at PID 40.
214 TMT-proteomics revealed a total of 6,015 proteins with more than two unique peptides, allowing

215 us to identify the top proteomic hits related to aging, aging/sAD and fAD-PSEN1 (Figures S3A
216 and S3B). Combining GO and integrated network analysis revealed the common, top-ranked
217 pathways altered by aging and AD, which include endosome-lysosome function, synapses,
218 chaperones, mitochondrial function, lipid signaling and inflammation (Figures 2E and S3C).
219 Comparing the proteomes of aged and young tNeurons identified age-related up-regulation of
220 proteins for modulating synaptic function (e.g. RAB27B and CADPS) and mitochondria (e.g.
221 HK2). In contrast, proteins for endosome-lysosomes (e.g. CLU, CD63, CTSC and TMEM175)
222 and chaperones (e.g. SACS) were mostly down-regulated with aging (Figure 2E). To evaluate
223 sAD-related changes, we compared the proteomes of aged/sAD and aged tNeurons and found
224 that the expression of proteins for endosome-lysosomes (e.g. CLU and TMEM175),
225 mitochondria (e.g. CHDH), inflammation (e.g. PYCARD and CRLF1) as well as synapses (e.g.
226 SORCS2) becomes enriched in aged/sAD tNeurons. We also observed down-regulation of
227 LGALS3BP and RAB27B, suggesting a deficit in membrane and vesicular trafficking in sAD
228 (Figure 2E). Since familiar PSEN1 mutations elicit early development of AD, we also examined
229 how fAD PSEN1 mutations affect the neuronal proteome versus that of aged/sAD derived
230 neurons. Comparative analyses showed that the components of the endosome-lysosome (e.g.
231 ABCA8, PLD3 and GALC), synapse (e.g. STON2) and membrane raft (e.g. AHNAK) pathways
232 are up-regulated in fAD-PSEN1. fAD-PSEN1 tNeurons also downregulated many mitochondrial
233 proteins, including mitoribosomes (Figure 2E). These proteomic analyses reveal that aging and
234 AD synergistically affect the architecture of the neuronal proteome by impacting organelle
235 homeostasis and proteostasis, thus suggesting a molecular rationale for the progressive
236 severity of amyloid and proteostasis phenotypes observed in aged and aged/sAD tNeurons.
237 Notably, proteins with changing expression in aged/sAD tNeurons were strongly associated with
238 the risk genes for AD (Figure 2F). This suggests that proteome changes in aged neurons may
239 synergize with risk gene mutations to bring about age-related neurodegenerative diseases.

240

241 Cluster analysis of our proteomic data further clarified how proteostasis pathways change
242 across young, aged, aged/sAD and fAD-PSEN1 tNeurons (Figure 2G). Major Clusters
243 implicated proteins collectively involved in proteolytic pathways, additional pathways
244 corresponded to autophagy, amyloid processing and translation. Comparing young, aged,
245 aged/sAD and fAD-PSEN1 tNeurons, we identified six proteolysis-related clusters of protein
246 trajectories, which ranged in size from 5 to 30 proteins. Cluster A reflected the relative
247 enrichment for proteins associated with fAD-PSEN1. Cluster B and C indicated the relative
248 enrichment for proteins in aged/sAD tNeurons, such as PYCARD and CTSC, whereas Cluster D
249 and F showed the relative enrichment for proteins in aged tNeurons, such as CTSK and
250 ERAP1. Notably, proteins in the autophagy pathway showed distinct trajectories of change for
251 aged/sAD. Cluster analysis of all protein whose abundance was altered across tNeurons
252 categories identified twelve clusters that exhibited distinct, yet concerted changes in biological
253 processes during normal aging and AD processes (Figure S3D).

254

255 Previous transcriptomic studies sowed that aging-related transcriptomic signatures can be
256 shared by multiple cell types or specific to a single cell type(Zhang et al., 2021). We thus asked
257 whether specific aging and AD proteome signatures are shared between the donor fibroblasts
258 and their matching tNeurons. These analyses revealed an overlap of pathways and protein hits
259 shared between human fibroblast and tNeurons but also cell-type-specific processes impacted
260 by aging and AD. We found 44 shared protein hits in the aging proteome and 33 shared
261 proteins in the aged/sAD proteome of both cell types (Figure 2H). For healthy aging, the
262 lysosome, ER and cytoskeleton pathways were similarly affected in both cell types, whereas the
263 axon and late endosome pathways were uniquely affected in neurons. For sAD, the lysosome
264 and ER pathways were commonly altered in both cell types, whereas proteins involved in

265 postsynaptic density and mitochondria matrix were specifically affected in neurons. These
266 results reveal that aging and AD can broadly impact the proteome of different cell types, but
267 also induce specific neuronal deficits.

268

269 **Defective responses to lysosomal damage emerge in aged and AD fibroblasts**

270 Proteomic analysis of human fibroblasts indicated that aging and aged/sAD affect the
271 endosome-lysosome pathway (Figures 1F, 1G and S1E). Cluster analysis provided a deeper
272 understanding of molecular signatures in the endosome-lysosome pathway across young, aged
273 and aged/sAD fibroblasts. For instance, ferritin (Cluster A) decreased in aging, whereas proteins
274 involved in lysosomal acidification (Cluster B) and lysosomal proteolysis and LQC (Cluster C)
275 (e.g. CHMP6 and LGALS8) were enriched in aging but decreased in sAD (Figures 3A and 3B).
276 These analyses were consistent with our finding that aged/sAD cells are highly sensitive to
277 lysosomal stress whereby CQ treatment of fibroblasts lead to strong accumulation of
278 autophagosome-interacting protein LC3B in aged/sAD cells (Figure S4A).

279

280 Based on these analyses, we next employed a battery structural and cell biological assays to
281 characterize the impact of aging and AD on lysosomal function in patient fibroblasts.
282 Transmission electron microscopy (TEM) showed that even under basal conditions, individual
283 lysosomes in aged/sAD fibroblasts are significantly larger than those in aged fibroblasts (by
284 50.7%, Figure 3C). To investigate the cellular response to lysosomal damage stress, fibroblasts
285 were treated with L-leucyl-L-leucine O-methyl ester (LLOME), a lysosomotropic compound that
286 is commonly used to induce lysosomal membrane permeabilization(Aits et al., 2015; Maejima et
287 al., 2013). LLOME induced lysosomal enlargement in all groups of fibroblasts (Figure 3C).
288 However, immunogold detection in TEM of lysosomal damage marker protein Galectin-3

289 showed it was frequently detected upon LLOME treatment of young and aged fibroblasts, but
290 barely in aged/sAD fibroblasts (Figure 3D), suggesting the potential dysregulation of lysosomal
291 damage response in AD.

292

293 Protein aggregates and pathogens are known factors to trigger damage to the lysosomal
294 membrane (Figure 3E). Leakage of intraluminal contents from ruptured lysosomes activates cell
295 death pathways, which are strongly associated with neurodegenerative diseases(Nixon et al.,
296 2008). Several pathways of LQC were recently identified as cytoprotective mechanisms to
297 resolve damaged lysosomes to avert cytotoxicity(Radulovic et al., 2018; Skowyra et al., 2018).
298 Mildly damaged lysosomes are repaired by successive recruitment of ESCRT proteins
299 (ESCRTs), whereas if the damage is severe, glycan-binding proteins, Galectins, bind to
300 glycosylated proteins residing in the lysosomal lumen and promote lysosomal clearance by
301 autophagy (i.e. lysophagy). In young healthy fibroblasts, LLOME-induced lysosomal damage
302 led to the expected time-dependent increase in ESCRT-III protein CHMP2B and Galectin-3
303 accumulation on lysosomes, leading to characteristic punctate structures (Figure 3E).
304 Scatterplots correlating the immunostaining intensity for CHMP2B and Galectin-3 showed these
305 puncta increased during LLOME treatment but were subsequently dissipated and reduced after
306 washout of the LLOME, as expected for lysosomal repair from damage (Figure 3F). We then
307 examined if the lysosomal damage response was different between healthy and diseased
308 fibroblasts. In young fibroblasts, CHMP2B-stained puncta became enriched during LLOME
309 treatment and rapidly dissipated after the LLOME washout. In contrast, aged and fAD-PSEN1
310 fibroblasts formed significantly higher number of CHMP2B puncta during LLOME treatment and
311 retained them for a longer time after washout (Figures 3G and S4B). Importantly, LLOME
312 treatment of aged/sAD fibroblasts led to lower densities of CHMP2B puncta on lysosomes,
313 suggestive of an impaired lysosome damage response. Indeed, a defective lysosomal damage

314 response in aged/sAD fibroblasts was also detected for additional ESCRT subunits, including
315 ESCRT-I TSG101, ESCRT-IIII CHMP1A and CHMP6 and ESCRT-III accessory factor ALIX
316 (Figure S4C). Further indicating deficits in lysosomal repair, the dynamics of Galectin-3
317 recruitment to lysosomes was also affected in aged and AD fibroblasts. LLOME treatment led to
318 higher levels of Galectin-3 puncta in aged and fAD-PSEN1 fibroblasts compared to young
319 healthy fibroblasts, as well as much slower dissipation rates during LLOME washout (Figures
320 3G and S4B). Of note, the Galectin-3 response to LLOME damage in aged/sAD fibroblasts was
321 more anomalous since high-density accumulation of Galectin-3 puncta was observed only 1 hr
322 after the LLOME washout, accompanied by slow dissipation of Galectin-3-puncta. Taken
323 together, these results indicate that aged and AD fibroblasts have a greater vulnerability to
324 lysosomal damage and likely due to deficits in LQC and recovery pathways.

325

326 We next asked if the dysregulated LQC in aged and AD fibroblasts is associated with enhanced
327 cytotoxicity. To this end, we evaluated the induction of cell death following the treatment using
328 two lysosome-damaging agents, LLOME and silica nanoparticles, with different mechanisms of
329 action (Figure 3H). LLOME-induced lysosomal membrane permeabilization is mediated by
330 lysosomal protease Cathepsin-C, while silica nanoparticles can directly damage the lysosomal
331 membrane and activate NLRP3 inflammasomes independent of Cathepsin-C(Mulay and
332 Anders, 2017; Skowyra et al., 2018). As compared with young fibroblasts, a 24-hr mild LLOME
333 treatment induced a moderate increase in cell death in aged and fAD-PSEN1 fibroblasts but a
334 dramatically rise in cell death in aged/sAD fibroblasts. Similarly, uptake of silica nanoparticles
335 led to a moderate increase in cell death in aged fibroblasts but a substantial increase in
336 aged/sAD and fAD-PSEN1 fibroblasts. These results indicate that aged/AD fibroblasts, which
337 have pronounced defects in LQC, are more prone to lysosomal damage-mediated cell death. In
338 addition to ESCRTs and Galectins, other proteostasis pathways participate in lysosome repair;

339 for instance, calcium homeostasis and the chaperone Hsp70 display essential roles in ESCRT
340 assembly and lysosomal stabilization(Kirkegaard et al., 2010; Scheffer et al., 2014). We find that
341 inhibition of calcium signaling by calcium chelator BAPTA-AM or Hsp70 function by VER-
342 155008 significantly perturbed LQC, impacting both CHMP2B and Galectin-3 recruitment during
343 LLOME treatment and dissipation after LLOME washout (Figure S4D). Consequently, both
344 calcium chelation and Hsp70 inhibition enhanced cell death associated with lysosomal damage
345 (Figure S4E). These results highlight the importance of chaperone function for LQC and
346 resonate with previous links between lysosomal calcium signaling and Hsp70 function with
347 AD(Lackie et al., 2017; Lee et al., 2015; Tong et al., 2018).

348

349 We next investigated how LQC deficits in aged and AD fibroblasts affect lysosomal function. To
350 assess the extent of lysosomal leakage following damage in these cells we preloaded
351 lysosomes with LysoTracker Red DND-99. LysoTracker Red fluorescence was significantly
352 increased in aged/sAD fibroblasts, indicative of lysosomal enlargement. LLOME treatment led to
353 loss of fluorescence, indicative of dye leakage from lysosomes, in all groups as expected from
354 lysosomal damage (Figure 3I). Because leakage of lysosomal protons will reduce lysosomal
355 acidification and intraluminal hydrolase activity, we next evaluated how lysosomes maintain or
356 repair these functions during and after damage. We measured lysosomal acidity changes in
357 fibroblasts using pH-sensitive, fluorescein (FITC)-conjugated Dextran (40 kDa). FITC-Dextran is
358 self-quenched in an acidic environment and increases fluorescence intensity upon
359 deacidification due to lysosomal damage (Figure S4F). At basal conditions, no obvious
360 endocytic deficiency was observed in aged and AD fibroblasts, assessed by an uptake of
361 tetramethylrhodamine (TMR)-conjugated dextran (70 kDa) (Figure S4F). Lysosomes of aged
362 and AD fibroblasts exhibited mild deacidification at the basal conditions (Figure 3J). Upon
363 damage, we found that young fibroblasts better resist pH perturbation and rapidly restore acidity

364 after lysosomal damage; in contrast aged fibroblasts showed intermediate acidity loss while AD
365 fibroblasts showed substantial lysosomal acidity loss and poor acidity recovery after damage.
366 Since lysosomal hydrolases, such as Cathepsins, are optimally active at pH 4-5, we used
367 Cathepsin-B substrates to measure changes in lysosomal proteolytic activity during lysosomal
368 damage. As expected, Cathepsin-B activity was dramatically lost in the presence of LLOME
369 (Figure 3K). One hr after LLOME washout, young fibroblasts were able to recover ~88% of
370 Cathepsin-B activity, whereas aged and AD fibroblasts only recovered ~68% and 45% of
371 activity, respectively. While the Cathepsin-B activity of young and aged fibroblasts was almost
372 fully recovered 8 hr after LLOME washout, AD fibroblasts restored less than 80% of Cathepsin-
373 B activity. We also examined the localization of transcription factor EB (TFEB), which
374 translocates to the nucleus upon lysosomal damage and activates the regulatory gene network
375 for lysosomal biogenesis(Settembre et al., 2011). While this was the case in young fibroblasts,
376 we observed a deficit in TFEB translocation into the nucleus following lysosomal damage in
377 aged/sAD fibroblasts (Figure S4G), perhaps due to aberrant nucleocytoplasmic transport in
378 AD(Eftekharzadeh et al., 2018). Interestingly, the delayed recovery from lysosomal damage in
379 AD fibroblasts may lead to detrimental effects beyond lysosomal dysfunction, as suggested by
380 recent proteomics analyses of damaged lysosomes(Eapen et al., 2021; Kravić et al., 2022).
381 Indeed, we find LLOME-damaged lysosomes do not only recruit ESCRTs and Galectins, but
382 also proteins involved in proteostasis (e.g. Hsp70), RNA processing (e.g. TDP43) and nuclear
383 pore complex (e.g. Nup98) (Figure 3L). Of note, calcium chelation by BAPTA-TA suppressed
384 the recruitment of ESCRTs and TDP-43 to the damaged lysosomes, but unexpectedly
385 enhanced Hsp70 association with lysosomes (Figure S4H). These results provide unprecedent
386 insights into how aging and AD increase lysosomal fragility and impair lysosomal repair, which
387 could jointly promote failures in proteostasis, lysosomal function and cell survival in AD patient
388 fibroblasts.

389

390 **Aging- and AD-linked deficits in lysosomal structure and repair are exacerbated in**
391 **tNeurons**

392 We next examined how fibroblast-to-tNeuron lineage reprogramming affects endosome-
393 lysosomal function. TEM comparison of lysosomal ultrastructure for young versus aged versus
394 aged/sAD tNeurons revealed a progressive increase in the size of individual lysosomes within
395 the cell body and proximal neurites from young to aged to aged/AD (Figure 4A). In addition, we
396 observed small electron-dense granules proximal to the lysosomal membrane in aged tNeurons
397 and large electron-dense granules in the swollen lysosomes of aged/sAD tNeurons. Strikingly,
398 the enlarged lysosomes within the cell body of aged/sAD tNeurons were closely surrounded by
399 mitochondria, suggesting increased mitochondria-lysosome contacts in AD neurons.

400

401 We next examined if lysosomal recovery from damage is also impaired in AD tNeurons as seen
402 in fibroblasts. Notably, even under basal conditions, we observed significantly higher number of
403 CHMP2B and Galectin-3 puncta in the lysosomes of aged/sAD tNeurons (Figures 4B, 4C, S5A
404 and S5B), consistent with spontaneously damaged lysosomes. Damage markers were less
405 frequently observed in young, aged and fAD-PSEN1 tNeurons. This suggests aging and AD
406 combine to create a synergistic deficit in lysosomal homeostasis in tNeurons. Interestingly, a
407 portion of aged/sAD tNeurons also showed aberrant accumulations of CHMP2B adjacent to the
408 plasma membrane and neurite branch points (Figure S5A), consistent with reports that
409 CHMP2B can participate in the repair of both plasma and lysosomal membrane
410 damage(Jimenez et al., 2014; Radulovic et al., 2018; Skowyra et al., 2018). There was no
411 significant difference in neuronal apoptosis at the baseline between groups (Figure S5C).

412

413 To understand the dynamics of lysosomal repair, we monitored the change in ESCRT-0 HGS
414 during LLOME treatment and washout. We chose ESCRT component HGS because its
415 distribution was comparable across all groups at baseline (Figures 4D and 4E). During LLOME
416 treatment, the number of HGS puncta moderately increased in aged tNeurons compared with
417 young tNeurons but substantially increased in aged/sAD and fAD-PSEN1 tNeurons. Monitoring
418 repair after LLOME washout showed that HGS puncta rapidly dissipate in young tNeurons
419 returning to baseline levels after 2 hr. In contrast, aged tNeurons exhibited a moderate delay in
420 the dissipation of HGS puncta while AD tNeurons exhibited a severe delay returning to baseline.
421 Relative to aged tNeurons, the half-life estimate of HGS granule dissipation increased by ~3-
422 fold in aged/sAD and ~1.5-fold in fAD-PSEN1 tNeurons (Figure 4E). Of note, we observed
423 recruitment of TDP-43 and Hsp70 to damaged lysosomes in aged tNeurons, which was further
424 exacerbated in aged/sAD tNeurons (Figure S5D), illustrating that deficits in lysosomal repair can
425 disturb additional proteostasis pathways.

426

427 We next examined lysosomal function in aged and AD neurons. Under basal conditions,
428 aged/sAD tNeurons exhibited a slight loss of lysosomal acidification which was exacerbated in
429 the presence of LLOME (Figure 4F). The enhanced lysosomal damage and reduced repair
430 observed in aged/sAD tNeurons was accompanied by reduced Cathepsin-B activity, indicative
431 of compromised lysosomal proteolytic function (Figure 4G). Since we observed spontaneous
432 formation of aberrant Aβ42 deposits in aged/sAD tNeurons (Figures 2D and S2D) and previous
433 finding showed Aβ preferentially accumulates in poorly acidified lysosomes at early AD
434 stages(Lee et al., 2022), we examined the relation of Aβ42 deposits with lysosomes in
435 tNeurons. Interestingly, we found Aβ42 colocalized with LAMP1 and LC3B in aged/sAD
436 tNeurons (Figure 4H), consistent with a link between lysosomal damage and amyloid
437 accumulation. Our data suggests that accumulation of damaged lysosomes in aged and AD

438 neurons leads to an overload of ESCRT and proteostasis systems, thus diminishing cellular
439 resilience to stress, and leading to increased accumulations of amyloid deposits and
440 susceptibility to neuronal cell death in AD.

441

442 **Lysosomal damage markers associate with amyloid pathology in brain tissue of AD**
443 **patients and mouse models**

444 To extend our observations from aged and AD derived tNeurons to brain tissues, we carried out
445 histopathological analysis of post-mortem cerebral cortex of AD patients and mouse models. In
446 sections of AD patients, we observed a global and intra-neuronal elevation of LAMP2, CHMP2B
447 and Galectin-3 immunoreactivity as compared with age-matched healthy control (HC)
448 individuals (Figures 5A and S5E). We observed two distinct patterns of CHMP2B staining in the
449 AD brain. While CHMP2B primarily colocalized with LAMP2-positive lysosomes in the
450 perinuclear region of neurons, we also observed thin thread-like CHMP2B-positive structures
451 with variable length and devoid of LAMP2 positivity in patient cerebral cortex. We also observed
452 increased colocalization of Galectin-3 with LAMP2 in the neurons of AD patients (Figures 5A
453 and S5E). Of note, Galectin-3 is highly up-regulated in microglia of AD patients brains and
454 5xFAD mice and strongly associated with amyloid plaques(Boza-Serrano et al., 2019; Grubman
455 et al., 2021). Also consistent with our finding that Aβ42 colocalizes with lysosomes in AD
456 tNeurons (Figure 4H), we observed Aβ deposits associated with LAMP2-positive lysosomes in
457 the extra-cellular and intra-neuronal plaques using 6E10 antibody in AD patient's cortex.

458

459 To explore how aging contributes to aberrant lysosomal signatures in the brain, we conducted
460 histological analysis of Galectin-3 and LAMP1 in the neocortex of young (3-6 month) and aged
461 (20-24 month) mice (Figure S6A). In aged mice, we observed a moderate increase in Galectin-3

462 immunoreactivity which colocalized with enlarged LAMP1-positive lysosomes in neurons (Figure
463 S6B). Together with our tNeuron analyses, these data implicate aging-linked lysosomal deficits
464 as contributing early factors to AD prior to neurodegeneration. Therefore, we examined
465 lysosomal and proteostasis pathologies in a mouse model for AD(Faizi et al., 2012). Transgenic
466 mice expressing human APP carrying Swedish (K670N/M671L) and London (V717I) mutations
467 (APPLon/Swe) exhibited a widespread accumulation of LAMP1-positive lysosomes in the
468 neocortex as compared with the non-transgenic (NTg) mice (Figures 5B, S6A, S6C and S6D).
469 Aberrant lysosomal accumulation forming various sizes of protein clumps and colocalizing with
470 lysosomal damage markers, such as CHMP2B and Galectin-3 (Figures 5B and S6C) and
471 chaperone Hsp70 (Figure S6D), were observed in the perinuclear region of individual pyramidal
472 neurons as well asthe extra-cellular space (Figure S6E). Similar to our findings in AD tNeurons,
473 the buildup of Aβ42-containing amyloid plaques was observed inside these lysosome clumps
474 (Figure 5B). Extra-cellular Aβ depositions were associated with an increase in the size of protein
475 clumps immuno-positive for CHMP2B and Galectin-3, as well as the severity of brain damage
476 regions devoid of MAP2 staining (Figures 5B, S6F and S6G). Of note, the pyramidal neurons of
477 APPLon/Swe mice proximal to Aβ plaques also contained intra-neuronal Aβ42 deposits within
478 lysosomes (Figure S6H). Taken together, the global increase in immunoreactivity of lysosomal
479 damage markers accompanying with co-aggregation with amyloid plaques and neuritic
480 degeneration suggest a critical role of lysosomal damage in the development of AD
481 neuropathology.

482

483 **Lysosomal damage potentiates inflammatory activation in AD tNeurons**

484 Our tNeuron proteomic datasets revealed that inflammasome adaptor protein PYCARD, also
485 referred to as ASC is up-regulated in aged/sAD tNeurons (Figure 6A). Inflammasomes are
486 multimolecular protein complexes involved in the innate immune response and composed of

487 NLRP3 (receptor), ASC (adaptor) and protease caspase-1 (effector). While NLRP3
488 inflammasomes are primarily activated in microglia as a pathogenic mechanism of AD(Heneka
489 et al., 2013), our data implicated this inflammatory response may also be upregulated in AD
490 neurons. We thus examined inflammasome activation via immunostaining of NLRP3 and ASC.
491 Under basal conditions, aged and fAD-PSEN1 tNeurons contained 2.7% inflammasome-
492 positive neurons per image field while aged/sAD tNeurons contained 4.6% inflammasome-
493 positive neurons per image field (Figure 6B).However, a 3-hr LLOME treatment led to
494 widespread activation of NLRP3 inflammasomes in tNeurons. Strikingly, the occurrence of
495 inflammasome-positive neurons was increased by 35-40% in aged/sAD tNeurons compared
496 with those of aged and fAD-PSEN1 donors. These results indicate that AD neurons possess a
497 relatively low-level inflammasome activation, but their high vulnerability to lysosomal damage
498 can lead to a potent activation of inflammasomes (Figure 6B).

499

500 We next examined whether tNeurons secrete inflammatory factors under basal and lysosomal
501 damage conditions. We thus compared cytokine secretion in the conditioned medium obtained
502 from tNeurons of young, aged, aged/sAD and fAD-PSEN1 donors (Figures 6C and 6D). To
503 assess if cytokine secretion is enhanced by lysosomal damage, we also compared the condition
504 medium of tNeurons of young donors with or without a low-dose LLOME treatment for 7 days
505 (Figures 6C and 6D) Cytokine profiling showed an age-dependent increase in levels of pro-
506 inflammatory cytokines (e.g. IL-6 and IFN-γ) and sAD-dependent increase in pro- and anti-
507 inflammatory cytokines (e.g. IL-1β, IL-4 and IL-15) and chemokines (e.g. CCL2 and CXCL12)
508 (Figures 6C and S7A). Importantly, extended treatment of young tNeurons with a low-dose of
509 LLOME increased the secretion of pro-inflammatory cytokines (e.g. IL-1β, IL-6 and IFN-γ) and
510 chemokines (e.g. CCL2) (Figures 6D and S7A). Pearson's correlation analysis identified a
511 moderate and positive correlation between total cytokine levels in the conditioned medium of

512 aged and aged/sAD tNeurons, as well as between young tNeurons treated with LLOME and AD
513 tNeurons (Figure 6E).

514

515 To put these observations in a disease relevant context, we examined cytokine expression in
516 existing human datasets and cerebrospinal fluid (CSF) samples. First, we examined cytokine
517 expression in single-nucleus RNA-seq analysis of neurons, astrocytes, microglia and
518 oligodendrocytes obtained from post-mortem cortex from HC donors. Cytokine and chemokine
519 transcripts were commonly found in neurons and glial cells. As expected, the transcript levels of
520 cytokines, chemokines and other inflammatory molecules are much higher in microglia than in
521 neurons (Figure 6F). Because CSF cytokines have been increasingly recognized as potential
522 biomarkers for diagnosing AD(Bettcher et al., 2018), we conducted an unbiased analysis of CSF
523 proteins in 50 HC and 29 AD donors in a search for biomarkers. Among them, we found higher
524 CSF levels of IL-15 and IL-20, and lower CSF levels of IL-1A, IL-1RA, VEGFA and TNFRSF6B
525 in AD than in HC (Figure S7B, Table S3). The increased concentration of IL-15 was previously
526 observed in CSF of AD patients and positively correlated with age of onset(Rentzos et al.,
527 2006). These data suggest that lysosomal dysfunction in aging and AD may lead to increased
528 secretion of a subset of cytokines that may serve as potential biomarkers of disease.

529

530 **Rescuing defective lysosomes ameliorates AD pathologies in fibroblasts and tNeurons**

531 An important question raised by our findings is whether aging and AD-linked lysosomal deficits
532 and vulnerabilities discovered in patient fibroblasts and tNeurons can be ameliorated by
533 pharmacological agents. Several small molecules have been shown to target specific aspects of
534 lysosomal homeostasis (Figure 7A). We previously identified a brain-penetrant lysosomal v-
535 ATPase complex activator, C381, that promotes lysosomal acidification. C381 can reduce

536 neuroinflammation, protein aggregates and neurodegeneration in mouse models of PD and
537 FTD(Vest et al., 2022). Another compound, thioperamide, increases a late endosomal and
538 lysosomal phospholipid, bis(monoacylglycero)phosphate (BMP), and rescues defects in
539 lysosomal lipid metabolism and membrane permeabilization in lysosomal storage
540 disorders(Moreau et al., 2019).

541

542 We tested whether C381 can ameliorate lysosomal dysfunction in human fibroblasts. Pre-
543 incubation of C381 at concentrations up to 12.5 μM for 24 hr reduced damaged lysosome-
544 mediated cell death in young, aged and AD fibroblasts (Figure 7B). We next examined if C381
545 reduces the loss of lysosomal acidification and proteolytic capacity upon LLOME treatment of
546 AD fibroblasts and subsequent recovery after LLOME washout (Figures 3J and 3K). Pre-treating
547 AD fibroblasts with 6.2 μM C381 improved their capacity to resist the loss of lysosomal
548 acidification and Cathepsin-B activity during LLOME treatment and accelerated the recovery
549 after LLOME washout (Figures 7C and 7D). Consistent with these functional recovery data,
550 C381 led to a dramatic reduction in number of CHMP2B and Galectin-3 puncta caused by
551 LLOME treatment (Figure 7E).

552

553 Next, we asked whether C381 ameliorates lysosomal deficits in tNeurons. First, we examined
554 the effect of pre-treatment of aged/sAD and fAD-PSEN1 tNeurons with 3.1 μM C381 for 7 days
555 on LLOME-mediated apoptotic cell death (Figure 7F). C381 was significantly neuroprotective
556 from LLOME-mediated apoptosis, and Caspase-3/7 activation by ~51% in AD tNeurons. As
557 observed in fibroblasts, C381 pretreatment reduced several aspects of lysosomal dysfunction in
558 neurons and improved their resilience to lysosomal damage. For instance, we find that aged
559 and aged/sAD tNeurons exhibited lower Cathepsin-B activity compared you young tNeurons,

560 even under basal condition (Figure 7G); the loss of Cathepsin-B activity is strongly exacerbated
561 by LLOME treatment, particularly for aged/sAD tNeurons. However, pre-treating tNeurons with
562 C381 restored Cathepsin-B activity to near-normal levels and ameliorated lysosomal proteolytic
563 deficits. Consistent with the improved recovery of lysosomal pH and proteolytic function, pre-
564 treatment of tNeurons with 3.1 μM C381 simultaneously reduced the number of detectable
565 CHMP2B and Galectin-3 puncta on lysosomes in aged and AD tNeurons by 15-39% and 34-
566 60%, respectively (Figure 7H).

567

568 The above analyses show that C381 preserves lysosomal functionality and facilitates the repair
569 of damaged lysosomes in aged and AD fibroblasts and tNeurons. We next investigated whether
570 improving lysosomal health impacts the AD-related pathologies observed in tNeurons, including
571 appearance of Aβ42 deposits (Figures 2D and S2D) and increased secretion of pro-
572 inflammatory cytokines (Figures 6C and S7A). Consistent wit lysosomal dysfunction leading to
573 accumulation of intra-neuronal Aβ42 levels, damaging lysosomal integrity by LLOME treatment
574 or blocking lysosomal repair with BAPTA-AM led to significant increases in intra-neuronal Aβ42
575 levels in aged/sAD and fAD-PSEN1 tNeurons (Figure 7I). Of note, LLOME had a marginal effect
576 on intra-neuronal Aβ42 levels in aged tNeurons. These experiments suggest that impairing
577 lysosomal function and repair beyond a specific threshold leads to Aβ42 accumulation. We next
578 tested if ameliorating lysosomal dysfunction by treating tNeurons with either C381 or
579 thioperamide ameliorates amyloid accumulation. Strikingly, both compounds significantly
580 reduced intra-neuronal Aβ42 levels, in aged tNeurons by ~32-36%, and AD tNeurons by ~34-
581 46%. Similar experiments causally linked lysosomal damage to inflammatory activation and
582 secretion of pro-inflammatory cytokines in AD tNeurons (Figures 6C, 6D and S7A). Thus,
583 amelioration of lysosomal damage by C381 treatment in aged/sAD and fAD-PSEN1 tNeurons
584 significantly reduced the secretion of pro-inflammatory cytokines (e.g. IL-6 and IL-15) and

585 chemokines (e.g. CCL2 and CXCL12) (Figures 7J and S7C). Taken together, these
586 experiments link the aging- and AD-related increase in lysosomal vulnerability and LQC
587 dysfunction to amyloid Aβ42 deposition and inflammatory cytokine secretion, and demonstrate
588 that improving lysosomal integrity and function has protective effects on aged/sAD and fAD-
589 PSEN1 neurons.
590

591 **DISCUSSION**

592 Here we address how aging and AD affect the human proteome using patient derived primary
593 fibroblast and their matching directly transdifferentiated tNeurons. These models have been
594 shown to preserve epigenetic and transcriptomic aging signatures(Huh et al., 2016; Mertens et
595 al., 2015; Miller et al., 2013). Our unbiased proteomic analyses were complemented and
596 extended by a battery of molecular and functional analyses. We find that aging and AD lead to
597 dramatic changes in several components of the proteostasis and organelle homeostasis
598 machinery. In particular, we identify the decline in endosome-lysosomal function and repair as a
599 cell-autonomous feature of sAD and fAD-linked mutations in PSEN1 gene. Deficits in lysosomal
600 repair lead to enhanced sensitivity to lysosomal damage stress in aged and AD. In neurons,
601 LQC defects are exacerbated, leading to damaged lysosomes even at basal conditions, which
602 predispose neurons to increased protein pathologies, such as intra-neuronal Aβ deposits,
603 inflammasome activation and cytotoxicity (Figure 7K). Consistent with our findings in tNeuron
604 models for AD, we identify massive accumulations of lysosomal damage markers across the
605 cerebral cortex of AD mice and patients, frequently colocalized with Aβ pathology. Finally, we
606 show that small molecules rescuing lysosomal pH regulation and integrity promote cellular
607 resilience to lysosomal damage and reduce both amyloid loads and pro-inflammatory cytokine
608 secretion in AD neurons. Importantly, our tNeuron models of aging and AD recapitulate AD-
609 related protein pathologies, including the spontaneous deposits of Aβ42 and p-Tau (Figures 2D
610 and S2D). These observations, together with our quantitative proteomic analyses support the
611 intrinsic dysregulation in proteostasis in AD neurons, and show it can lead to amyloid deposits
612 without seeding or overexpression of human disease proteins. Overall, this study demonstrates
613 the utility of transdifferentiation of fibroblasts from AD patients to neurons as a valuable
614 approach to understand molecular mechanisms of aging and AD and to advance
615 neurodegenerative disease therapeutic approaches.

616 **Proteomic and proteostasis signatures in aging and AD**

617 Our analyses reveal cellular proteome changes in human cell models of aging and AD. Of note,
618 such cytosolic and organelle-specific proteostasis changes are often not apparent from genomic
619 and transcriptomic data(Laskowska et al., 2019). Proteomic analyses of donor fibroblasts
620 indicate an age-dependent up-regulation of LQC proteins and and AD-dependent down-
621 regulation of v-ATPases (Figures 1F, 1G and 3A). In tNeurons, the levels of lysophagy-related
622 proteins were altered in aging (e.g. CNN2, HspB1) and AD (e.g. DPP7, PLBD2, PLD3, TAGLN)
623 (Figure 2E)(Eapen et al., 2021; Kravić et al., 2022). Our proteomic and functional analyses
624 inAD tNeurons highlight the functional interconnection between endosome-lysosomal,
625 proteostasis and inflammation subcellular systems. While the interconnectivity of different
626 quality control pathways establishes robustness and adaptability under normal conditions, the
627 impairment in one of these subsystems, for instance due to aging or disease-mutation, can drive
628 a cascade of decline to inter-connected subsystems (Gottschling and Nyström, 2017; Petkovic
629 et al., 2021). We propose that such a vicious cycle of dysfunction may contribute to the
630 synergistic defects observed for aging and AD in our cell models. Our data comparing two cell
631 types also suggest that neurons are particularly vulnerable to this cycle of homeostatic decline,
632 thus underlies their sensitivity to aging and mutation and their higher incidence of protein
633 pathologies accompanying cellular death.

634

635 Intriguingly, we find that AD patient fibroblasts exhibit an increased tendency to lysosomal
636 damage in absence of protein pathology. However, the more severe level of lysosome damage
637 in aged/sAD tNeurons is accompanied by protein deposits. Of note, the intracellular Aβ deposits
638 were significantly higher in fAD-PSEN1 than aged/sAD tNeurons. These lines of evidence
639 suggest that aging, genetic mutations and stochastic disease factors synergistically and
640 adversely impact lysosomal repair and recovery after damage; and beyond a threshold, this

641 may lead to a cell-autonomous mechanism for neurodegeneration in AD. While, defective
642 autophagy in microglia has been extensively studied and linked to AD pathogenesis (Wang et
643 al., 2022); the role of neuronal autophagy in this pathological event is less understood. Neurons
644 are particularly sensitive to lysosomal dysfunction compared with other types of brain cells (Tian
645 et al., 2021). Of note, lysosomes are interconnected hubs linked to both proteostasis and
646 homeostasis of other organelles (such as mitochondria and ER), it is clear to envision how such
647 deficits impair cell survival. Since internalized aggregated proteins are thought to be an
648 important mechanism of endosome-lysosomal membrane rupture(Ditaranto et al., 2001; Jiang
649 et al., 2017), the presence of protein pathologies likely enhances further lysosome dysfunction.
650 Previous studies found that the depletion of lysosomal repair factors, such as ESCRT-III
651 subunits or PI4K2A, in immortalized cell lines impacts lysosomal stability and causes an escape
652 of tau fibrils from lysosomes to trigger cytoplasmic aggregation (Chen et al., 2019; Tan and
653 Finkel, 2022). The knockdown of ESCRTs or expression of mutant VPS4A enhanced
654 intracellular Aβ accumulation and endosomal membrane lesion, mimicking AD pathogenesis
655 (Fruhmann et al., 2018; Willén et al., 2017). Hence, our work provides a direct link between
656 defective LQC and AD neuropathology (Figure 7K). The failure to resolve lysosomal damage in
657 conjunction with other well-studied autophagy-lysosomal defects can collectively contribute to
658 AD pathogenesis(Cortes and La Spada, 2019; Whyte et al., 2017; Wolfe et al., 2013).

659

660 **Genetic risk factors link to endosomal and autophagy-lysosomal dysfunction in neurons**

661 Our proteomic analyses resonate with GWAS studies identifying AD casual genes and risk
662 genes for late-onset AD to the endosomal and autophagy-lysosomal pathway, such as BIN1,
663 CLU, GRN, PICALM, PLD3 and SORL1(Zhang et al., 2022). We find PSEN1 mutations
664 promote defects in lysosomal acidification and increase susceptibility to lysosome-mediated
665 death. Our data is consistenty with, and explains, a number of previous studies. PSEN1

666 pathogenic mutations or knockout impair lysosomal v-ATPase assembly and autophagosome-
667 lysosome fusion and elevate Aβ42/40 ratio (Hung and Livesey, 2018; Kwart et al., 2019; Lee et
668 al., 2015; Lee et al., 2010). A recent study characterized different transgenic mouse models for
669 AD and identified accumulation of APP-βCTF/Aβ in poorly acidified lysosomes of cortical
670 neurons as a very early event in AD (Lee et al., 2022). Before amyloid deposits were observed,
671 neurons had developed low v-ATPase activities, lysosomal acidification deficits and higher
672 membrane permeabilization in mouse and Braak-stage-II human brains. The build-up of APP-
673 βCTF/Aβ in the perinuclear deacidified lysosomes progressed with age, consistent with our
674 findings. Our findings further implicate intraneuronal accumulation of amyloid peptides resulting
675 from neuronal lysosomal defects as the origin of extracellular amyloid plaques in the brain
676 (Gouras et al., 2000; Masters et al., 1985; Mochizuki et al., 2000).

677

678 **Lysosomal pathology links to GVD and neuroinflammation in AD**

679 The presence of cytoplasmic granule-containing vacuoles is a neuropathological feature of GVD
680 in AD(Köhler, 2016). Similar to our findings in cells, GVD bodies structurally resemble endocytic
681 and autophagic vesicles and contain various proteins, including the typical hallmarks CHMP2B,
682 LAMP1 and CK1δ, proteins involved in endocytosis (CHMP1A) and proteostasis (Hsp70), and
683 AD-related amyloidogenic proteins, such as Aβ, pTau and TDP-43(Hondius et al., 2021). Thus,
684 our analyses of AD tNeurons as well as human and mouse brain sections suggested lysosomal
685 damage underlying GVD etiology in AD.

686

687 Our study indicates that loss of lysosomal integrity in neurons plays critical roles in
688 inflammasome activation in pathological conditions. Consistent with this observation, a recent
689 study indicated the senescence-like neurons may be a novel source of neuroinflammation in AD

690 (Herdy et al., 2022). Previous findings also indicate lysosomal membrane permeabilization in
691 microglia activates NLRP3 inflammasomes and promotes the secretion of pro-inflammatory
692 cytokines, thus aggravating neuronal damage(Wang et al., 2017). Our cytokine profiling of
693 conditioned medium from AD tNeurons revealed that the increased secretion of pro-
694 inflammatory cytokines is associated with chronic lysosomal damage. Human CSF proteomics
695 further supported IL-15 as the potential biomarker for AD (Figure S7B).

696

697 **Comparing transdifferentiated neurons with iPS cell-derived neurons**

698 One key finding in our study is that aging-linked proteostasis and organelle homeostasis
699 impairment sensitizes cells, particularly neurons, to further damage due to stochastic AD events
700 or to AD-causing mutations. These findings are enabled because directly transdifferentiated
701 neurons retain aging signatures while stem cell reprogramming has demonstrated a remarkable
702 ability to rejuvenate cells by reversing age-related global changes (Mahmoudi and Brunet,
703 2012). Many lines of evidence indicate that cell-based models of age-dependent
704 neurodegenerative diseases benefit from retaining these aging marks. In Huntington's disease,
705 mutant huntingtin aggregates are often detected in human tNeurons and post-mortem tissue,
706 but rarely in iPS cell-derived neurons from the fibroblasts of same patient cohorts(Victor et al.,
707 2018). Similarly, tNeurons from donors harboring the FTD-linked MAPT IVS10+16 mutation
708 produced more aggregation-competent tau than iPS cell-derived neurons from the same
709 donors(Capano et al., 2022). These lines of evidence highlight the importance of aging in the
710 manifestation of proteostasis dysfunction. Transcriptomic and proteomic analysis of iPS cell-
711 derived neurons derived from sAD patients reported increased expression of genes and
712 proteins involved in synaptic vesicle regulation and microtubule organization and exhibited
713 pathological signatures of increased synaptic loss, Aβ42 levels and reactive oxygen species
714 production(Birnbaum et al., 2018; Israel et al., 2012; Lagomarsino et al., 2021; Zhao et al.,

715 2020). However, the iPS cell-derived sAD neurons did not reveal the strong disease- and aging-
716 related changes in proteostasis and lysosomal homeostasis observed with tNeurons. Since sAD
717 tNeurons and iPS cell-derived neurons both show an elevated expression of synaptic proteins,
718 perhaps synaptic dysregulation is an early, hyper-vulnerable event that is faithfully reflected by
719 both neuronal models, while proteostasis and organelle homeostasis deficits require the
720 contribution of aging.

721

722 **Pharmacological rescue of lysosomal deficits ameliorates AD neuropathology**

723 Our data suggests that drugs targeting lysosomal function may provide potential therapeutic
724 benefit to aging and AD. Lysosomal dysfunction is commonly observed across
725 neurodegenerative diseases and several strategies for improving autophagy-lysosomal function
726 have been tested in different model systems(Cao et al., 2021b). Thus, loss of lysosomal
727 acidification is central to aging and to several forms of neurodegenerative diseases and
728 neuronal ceroid lipofuscinosis. Based on these findings, targeting lysosomal acidification has
729 become a desired strategy. Re-acidifying lysosomes by v-ATPase-targeting compounds (for
730 example, EN6 and C381) or endocytosed nanoparticles (for example, PLGA-aNP and NP-1)
731 showed promising effects on promoting the clearance of protein aggregates, rescue of
732 autophagic dysfunction and attenuation of neuroinflammation and neurodegeneration in
733 different pathological contexts(Bourdenx et al., 2016; Chung et al., 2019; Lee et al., 2015; Vest
734 et al., 2022). The v-ATPase-targeting compound, C381 can rescue deficits in lysosomal
735 acidification and disease-relevant pathologies in both neurons and glial cells in disease models
736 for AD, PD and FTD. Further, C381 is orally bioavailable and brain penetrant, reflecting good
737 translational potential (Vest et al., 2022). Administration of mTOR inhibitor, rapamycin, was
738 shown to reduce neuropathology in mouse models for AD (Talboom et al., 2015), although its
739 associated immunosuppression effects reduces translation potential for AD. A large-scale drug

740 screening for mTOR-independent autophagy activators identified additional molecules that
741 promotes tau and Aβ clearance in neuronal models for AD and FTD(Yoon et al., 2022).
742 Moreover, ameliorating lysosomal membrane permeabilization prevents inflammatory
743 responses and cell death. Overexpression or exogenous administration of Hsp70 stabilized
744 lysosomes against membrane rupture in patient fibroblasts of Niemann-Pick disease(Kirkegaard
745 et al., 2010). Peripheral delivery of progranulin exhibited a promising effect on the correction of
746 BMP deficiency and reduction of lysosomal damage and dysfunction, lipofuscinosis and
747 inflammatory responses in the mouse model for FTD(Logan et al., 2021). Despite these
748 promising avenues, compounds that directly enhance lysosomal repair have not yet been
749 reported. One of the reasons is that these repair processes involve the concerted recruitment of
750 more than 30 proteins, including ESCRT and proteostasis factors to determine the timing and
751 hierarchy of events leading to membrane curvature, scission and fusion. The depletion of single
752 ESCRT subunit affects lysosomal repair, whereas the overexpression of single subunit has no
753 obvious improvement(Skowyra et al., 2018). Future studies leading to discovery of small
754 molecules that accelerate lysosomal repair may exert beneficial effects for treating
755 neurodegenerative diseases.

756

757 **Study limitation:** Our study uses monocultures of tNeurons without glial cell support and short-
758 term culture conditions (i.e. 5-6 weeks) which are quite distinct from the complex tissue
759 organization and prolonged aging processes in human brain. Thus, our cell-based models may
760 not entirely reflect the physiological signatures of aging and pathology of AD. The neurons were
761 derived from human adult fibroblasts of several donors to strive to account for patient
762 heterogeneity. The challenging conversion and cell culture system limits the experimental
763 scalability for larger donor cohort sizes and large-scale biochemical analyses. In addition, the
764 healthy young and aged fibroblasts were collected from donors who are clinically normal at that

765 moment, but we cannot rule out their possibility for developing dementia due to AD after
766 decades. Finally, it will be important to determine the mechanism of action of lysosome-
767 targeting compounds and investigate how these compounds change cell proteomes and
768 promote lysosomal activation.
769

Acknowledgements:

We thank Stanford Alzheimer's Disease Research Center (ADRC), D. Channappa and M. Greicius with kind support for collecting and identifying human fibroblast lines, post-mortem brain tissue and CSF samples. Y. Rosenberg-Hasson and J. Liang from Stanford Human Immune Monitoring Center for help with cytokine profiling; J. Perrino from Stanford Cell Sciences Imaging Core Facility for help with TEM experiments; P. Chu from Stanford Human Pathology/Histology Service Center for help with tissue processing; M. Weglarz from Stanford Shared FACS Facility for FACS support. We thank T.K. Rainbolt, V.B. Masto and S. Taguwa of the Frydman laboratory for helpful discussions on experimental design; J. Kelly, R.I. Morimoto, S. Finkbeiner and D. Gate for helpful inputs to the manuscript. This work was supported by NIA P01AG054407 (J.F., D.F. & J.W.K.) and the Michael J. Fox Foundation for Parkinson's Research and the Aligning Science Across Parkinson's (ASAP) initiative (J.F.). The Michael J Fox Foundation administers the grant ASAP-000282 on behalf of ASAP and itself; the Glenn Foundation for Medical Research Postdoctoral Fellowship in Aging Research (C.-C.C.), the Life Sciences Research Foundation Postdoctoral Fellowship (C.-C.C.) and the Alzheimer's Disease Research program in BrightFocus Foundation Grant (C.-C.C.); the NIA-funded Stanford ADRC P50AG047366 and P30AG066515 (T.W.-C. & P.M.L.); the Goldberg Fund Fellowship and the Miguel Servet Program (CP21/00017) (M.A.P.).

Author contributions:

C.-C.C. and J.F. conceptualized the study, designed experiments, interpreted data and wrote the manuscript with inputs from all authors. C.-C.C. conducted cell culture, immunofluorescence staining, microscopy, flow cytometry, conditioned medium experiments with the help of T.-T.L.. C.-C.C. performed transdifferentiation with the help of Y.S. under the supervision of M.W.. C.-C.C., R.V. and J.L. carried out mice and drug experiments under the supervision of T.W.-C.. M.A.P. and J.W.-G. set up the proteomic data-processing pipelines and performed bioinformatic data analysis with the help of C.-C.C. and J.A.P. under the supervision of S.P.G. and D.F.. P.M.L. processed and analyzed human CSF data under the supervision of T.W.-C.. J.W.K. provided key reagents and helped design lysosome function assays. All authors read and approved the manuscript.

Declaration of interests:

R.V., J.L. and T.W.-C. are co-founders of Qinotto Inc.

FIGURES AND FIGURE LEGENDS

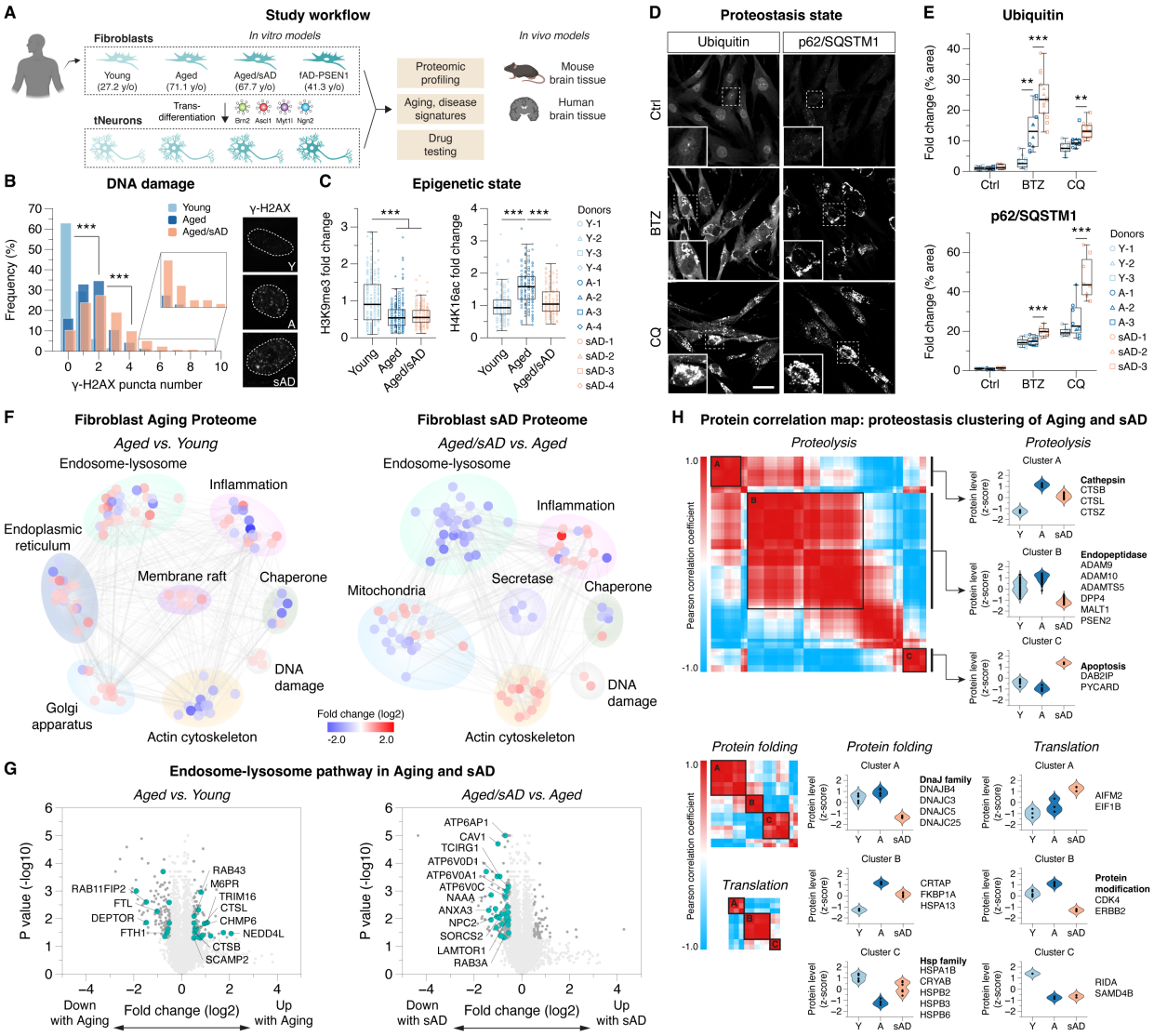

Figure 1 Molecular and quantitative proteomic analysis identify signatures of aging and Alzheimer's disease (AD) in human adult fibroblasts.

(A) Experimental layouts for this study. Human fibroblasts are collected from donors of healthy young and aged, aged with sporadic AD (aged/sAD) and familial AD with PSEN1 mutations (fAD-PSEN1). Fibroblasts and transdifferentiated neurons (tNeurons) are used for molecular and proteomic characterization of aging and disease signatures and tested for cellular responses to small molecules. Validation of cellular findings is performed in post-mortem brain tissue from AD mouse models and patients.

813 (B) Levels of DNA damage measured by increased numbers of the nuclear foci of γ-H2AX
814 immunocytochemistry shown in the representative images of human fibroblasts.

815 (C) Age- and AD-related epigenetic alterations measured by histone modifications H3K9me3
816 and H4K16ac immunocytochemistry in human fibroblasts.

817 (D) Representative images of endogenous ubiquitin and p62/SQSTM1 in young fibroblasts
818 treated with DMSO control (Ctrl), Bortezomib (BTZ, 25 nM) or Chloroquine (CQ, 25 μM) for 24
819 hr. Insert: higher magnification view of ubiquitin and p62/SQSTM1. Scale bar: 40 μm.

820 (E) Quantification of proteostasis markers shown in panel (D) for detecting changes in ubiquitin
821 and p62/SQSTM1 under proteasomal and autophagic stress caused by the treatment of BTZ
822 and CQ, respectively, in young, aged and aged/sAD fibroblasts.

823 (F) Network analysis of fibroblast proteomes including proteins in the top-ranked pathways
824 associated with aging and sAD by GeneMANIA and Gene ontology (GO). Comparison between
825 the fibroblasts from aged and young donors (Aging proteome) and between the fibroblasts from
826 aged/sAD and aged donors (sAD proteome). Colored circles represent the enrichment of
827 identified proteins revealing by log2-fold change: increase in red and decrease in blue.

828 (G) Volcano plots showing differentially expressed proteins in the endosome-lysosomal
829 pathway. The plots display the log2-fold change (x-axis) and -log10 statistical P value (y-axis).
830 Proteins with significantly changed levels are shown in dark grey. Among them, the endosome-
831 lysosomal proteins are labeled in blue-green color.

832 (H) Clustering representation based on the Pearson correlation of the enrichment of fibroblast
833 proteins in the proteostasis pathways. GO analysis of the differentially expressed proteins,
834 defined by the relative protein abundance (z-score), reveals the top proteostasis terms
835 associated with aging and sAD, including proteolysis, protein folding and translation. Black dots
836 within the violin graph represent the expression levels of individual proteins in each group.

837 Data show box-and-whisker plots of 2 to 4 independent experiments and cells from independent
838 healthy control (HC) and AD donors. Box-and-whisker plots depict 5th, 25th, 50, 75th and 95th
839 percentiles. Differences between groups are compared with One-Way ANOVA followed by
840 Bonferroni post-hoc analysis. **$P < 0.01$ and ***$P < 0.001$.

841 See also Figure S1 and Table S1.

842

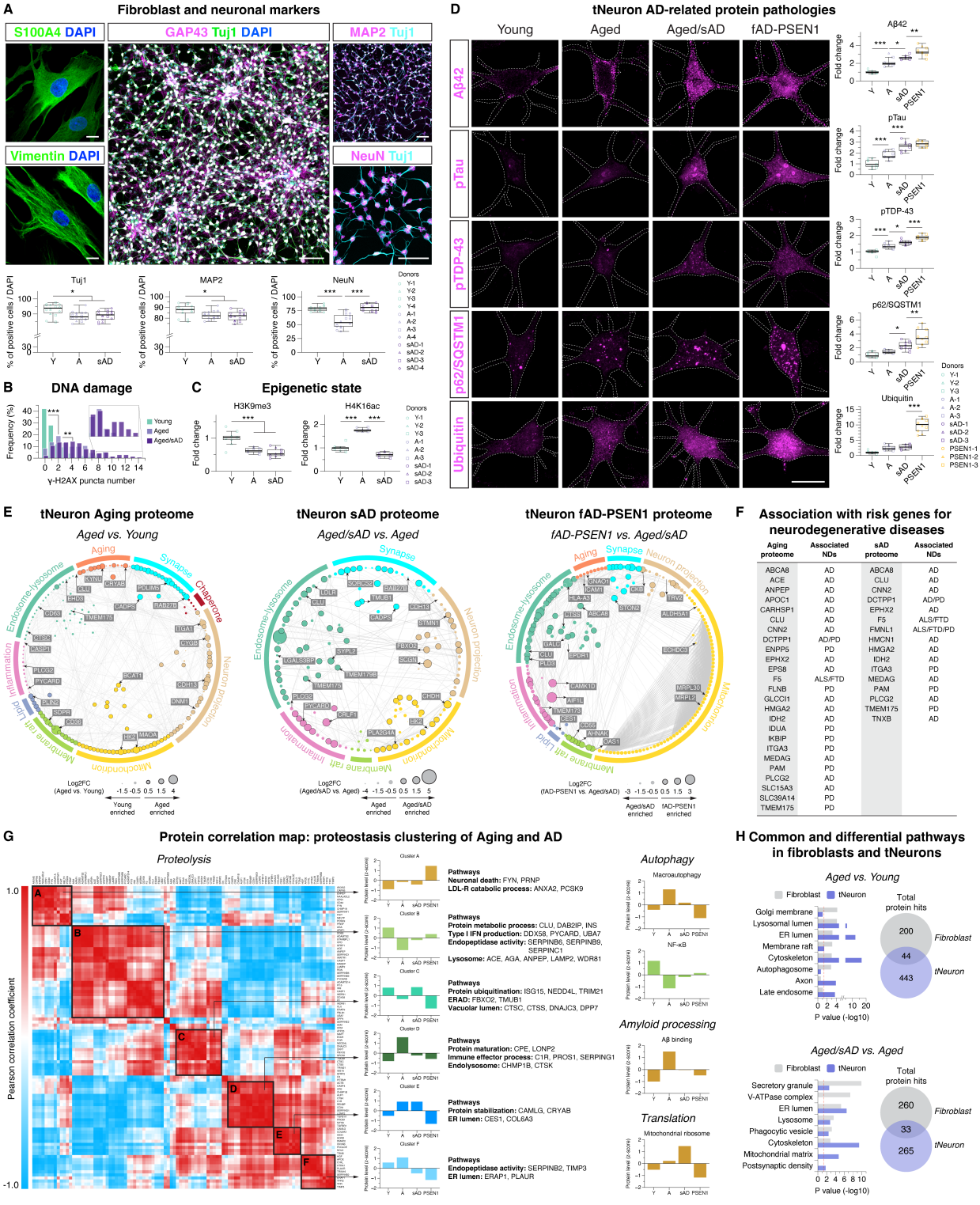

Figure 2 Human tNeurons carry molecular and proteomic signatures of aging, sAD and fAD harboring PSEN1 mutations.

846 (A) Representative images of human fibroblasts immunostained for S100A4 and Vimentin, and
847 tNeurons immunostained for GAP43, Tuj1, MAP2 and NeuN with DAPI counterstaining.
848 Quantification of Tuj1-, MAP2- and NeuN-positive cells at post-induction day (PID) 35. Scale
849 bar: 100 μm.

850 (B) Measurement of DNA damage in tNeurons quantified by numbers of the nuclear foci of γ-
851 H2AX immunocytochemistry.

852 (C) Measurement of immunocytochemical changes in histone modifications H3K9me3 and
853 H4K16ac in tNeurons.

854 (D) Representative images and quantification of proteostasis- and disease-associated protein
855 markers in tNeurons, including amyloid-β 42 (Aβ42), hyper-phosphorylated tau (pTau) and TDP-
856 43 (pTDP-43), autophagy adaptor p62/SQSTM1 and ubiquitin. Scale bar: 20 μm.

857 (E) Differential expression of proteins detected in tNeurons from healthy young (n = 3) and aged
858 (n = 3) individuals, and patients with sAD (n = 6) and fAD-PSEN1 (n = 2) at PID 40. The top
859 pathways for aging, sAD and fAD-PSEN1 proteomes are analyzed using GO databases and
860 annotated in color. The aging proteome is reflected by comparing proteomic data between aged
861 and young, the sAD proteome by comparing between aged/sAD and aged, and the fAD-PSEN1
862 proteome by comparing between fAD-PSEN1 and aged/sAD. The size of the filled circles
863 reflects log2-fold change. A circle with a thick black outline indicates that the protein is enriched
864 in aged (Aging proteome), aged/sAD (sAD proteome) and fAD-PSEN1(fAD-PSEN1 proteome)
865 tNeurons. Protein name with underline represents the previously known protein associated with
866 AD.

867 (F) List of differentially expressed proteins associated with the risk genes for age-related
868 neurodegenerative diseases. AD: Alzheimer's disease. PD: Parkinson's disease. ALS/FTD:
869 Amyotrophic lateral sclerosis and frontotemporal dementia.

870 (G) Clustering heatmap of Pearson correlation coefficients of tNeuron protein expression in the
871 proteostasis pathways. Top GO terms associated with aging and AD, including proteolysis,
872 autophagy, amyloid processing and translation. In the proteolysis term, Cluster A to F show
873 distinct protein expression patterns and the differentially expressed protein lists, defined by the
874 relative protein abundance (z-score) across young, aged, aged/sAD and fAD-PSEN1 group. Bar
875 graph represents the average expression levels of proteins in each group.

876 (H) Diagram identifying aging- and AD-related protein hits and pathways that are unique to or
877 shared by human fibroblasts and tNeurons.

878 Data show box-and-whisker plots of 2 to 4 independent experiments and cells from independent
879 HC and AD donors. Box-and-whisker plots depict 5th, 25th, 50, 75th and 95th percentiles.
880 Differences between groups are compared with One-Way ANOVA followed by Bonferroni post-
881 hoc analysis. *P < 0.05, **P < 0.01 and ***P < 0.001.

882 See also Figure S2, Figure S3 and Table S2.

883

884

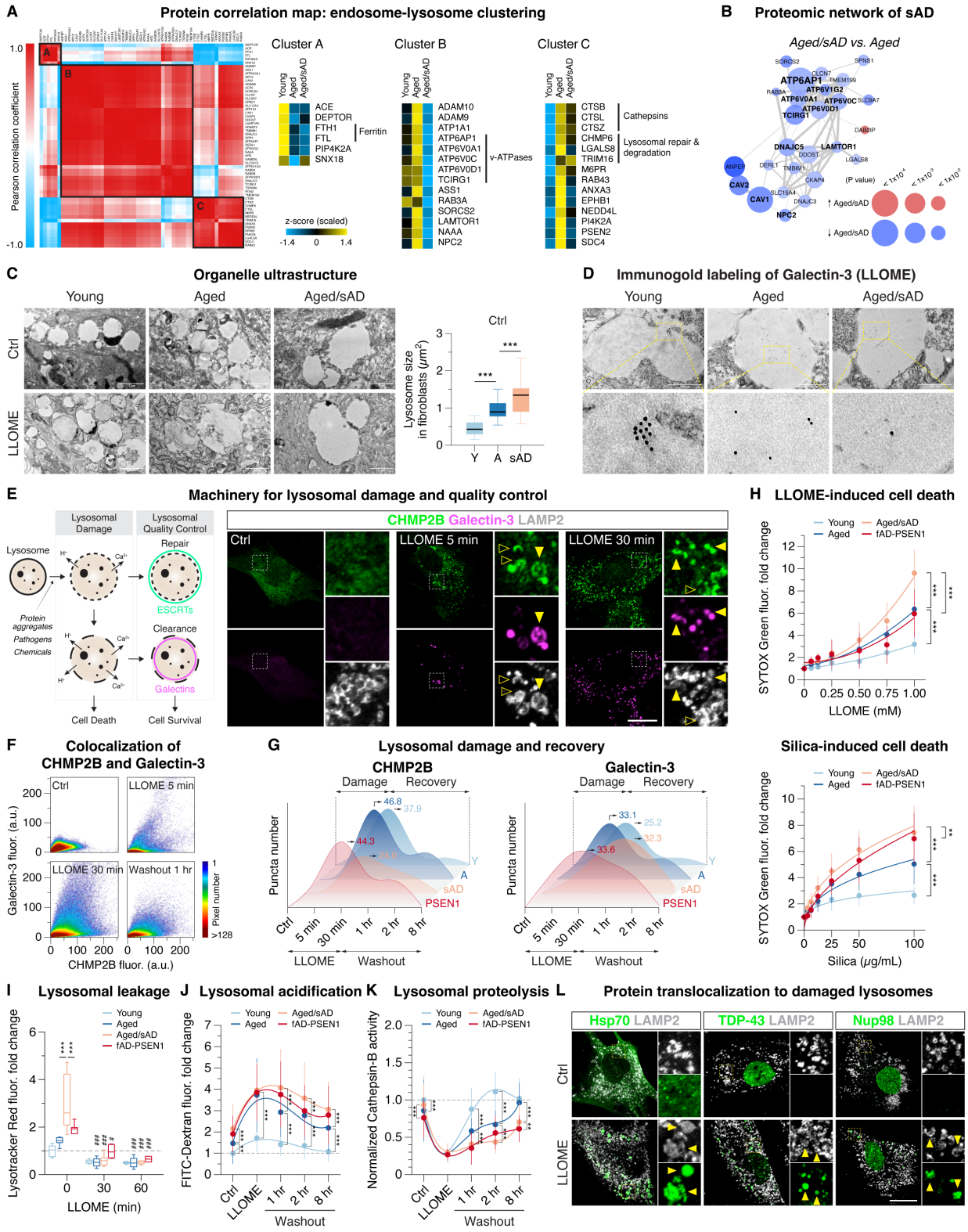

Figure 3 Defects in lysosomal quality control (LQC) exacerbate lysosomal dysfunction and cell death in AD fibroblasts.

888 (A) Clustering heatmap of Pearson correlation coefficients of the fibroblast protein expression in
889 the endosome-lysosomal pathway. Cluster B and C show the reduction in the relative
890 abundance of proteins involved in lysosomal pH regulation (Cluster B), and lysosomal
891 proteolysis and LQC (Cluster C) in aged/sAD fibroblasts.

892 (B) Network of fibroblast proteins and the relative abundance in the endosome-lysosomal
893 pathway. Protein abundance increases in aged/sAD shown in red and decreases in blue. The
894 circle size is represented by -log10 statistical P value.

895 (C) Transmission electron microscopy (TEM) for analyzing the ultrastructural morphology of
896 lysosomes in fibroblasts. Experiments were performed in 2 cell lines from each group and
897 repeated twice independently. Scale bar: 1 μm.

898 (D) Immunogold staining of lysosomal damage marker Galectin-3 for TEM in fibroblasts treated
899 with 1 mM LLOME for 10 min reveals Galectin-3 translocation to the damaged lysosomes.
900 Experiments were performed in 2 cell lines from each group and repeated twice independently.
901 Insert: higher magnification view of gold particles. Size of gold particles: 10 nm. Scale bar: 500
902 nm.

903 (E) Schematic for LQC machinery. While undergoing lysosomal damage stress, the lysosomal
904 membrane is subjected to rupture. Lysosomes recruit ESCRT proteins (ESCRTs) to repair the
905 mildly damaged membrane and Galectins to target the massively damaged lysosomes for
906 lysophagy. Immunostaining of ESCRT-III protein CHMP2B (green), Galectin-3 (magenta) and
907 lysosome-associated membrane protein LAMP2 (grey), during different time courses of
908 lysosomal damage caused by 1 mM LLOME treatment. Insert: higher magnification view of
909 CHMP2B, Galectin-3 and LAMP2. Hollow arrowhead: colocalization of CHMP2B and LAMP2.
910 Solid arrowhead: colocalization of CHMP2B, Galectin-3 and LAMP2. Scale bar: 20 μm.

911 (F) 2D Histogram shows the colocalization patterns of CHMP2B (x-axis) and Galectin-3 (y-axis)
912 immunofluorescence in young fibroblasts during 1 mM LLOME treatment and washout. Each
913 dot means the pixel intensity in both CHMP2B and Galectin-3 channels of the image.

914 (G) Plot profiles represent the dynamics of CHMP2B and Galectin-3, indicated by the changes
915 in puncta number as shown in panel (E), in fibroblasts of young (Y), aged (A), aged/sAD (sAD)
916 and fAD-PSEN1 (PSEN1) donors during 1 mM LLOME treatment and washout. The puncta
917 number represents the tendency of lysosomes toward damage and the efficiency of lysosomal
918 recovery from damage.

919 (H) Lysosome-mediated death in fibroblasts caused by the treatment of LLOME (upper) or Silica
920 nanoparticles (bottom) for 24 hr, detected by the SYTOX Green assay. The SYTOX Green
921 intensities are normalized to Hoechst and divided by the data with no compound treatment as
922 fold change.

923 (I) The detection of leakage of intraluminal contents from fibroblast lysosomes during 1 mM
924 LLOME treatment.

925 (J) Changes in lysosomal acidification, indicated by the pH-sensitive Fluorescein isothiocyanate
926 (FITC)-conjugated Dextran, in fibroblasts during 1 mM LLOME treatment for 30 min and after
927 washout for up to 8 hr, revealing the functional recovery of lysosomes after damage.

928 (K) Measurement of lysosomal proteolytic capacity by monitoring the lysosomal protease
929 Cathepsin-B activity of fibroblasts during 1 mM LLOME treatment for 30 min and washout.

930 (L) Immunostained fibroblasts for endogenous Hsp70, TDP-43 and Nup98 in the presence of
931 1mM LLOME. Insert: higher magnification view of Hsp70, TDP-43 and Nup98 and LAMP2.
932 Yellow arrowhead: protein colocalization with LAMP2. Scale bar: 20 μm.

933 Data show mean and SD or box-and-whisker plots of 3 to 8 independent experiments and 3 cell
934 lines from independent HC and AD donors. Box-and-whisker plots indicate 5th, 25th, 50, 75th
935 and 95th percentiles. Differences between groups are compared with One-Way or Two-Way
936 ANOVA followed by Bonferroni post-hoc analysis. *P < 0.05, **P < 0.01 and ***P < 0.001. #P <
937 0.05 and ###P < 0.001 as comparing to 0 min of each group in panel (I).

938 See also Figure S4.

939

940

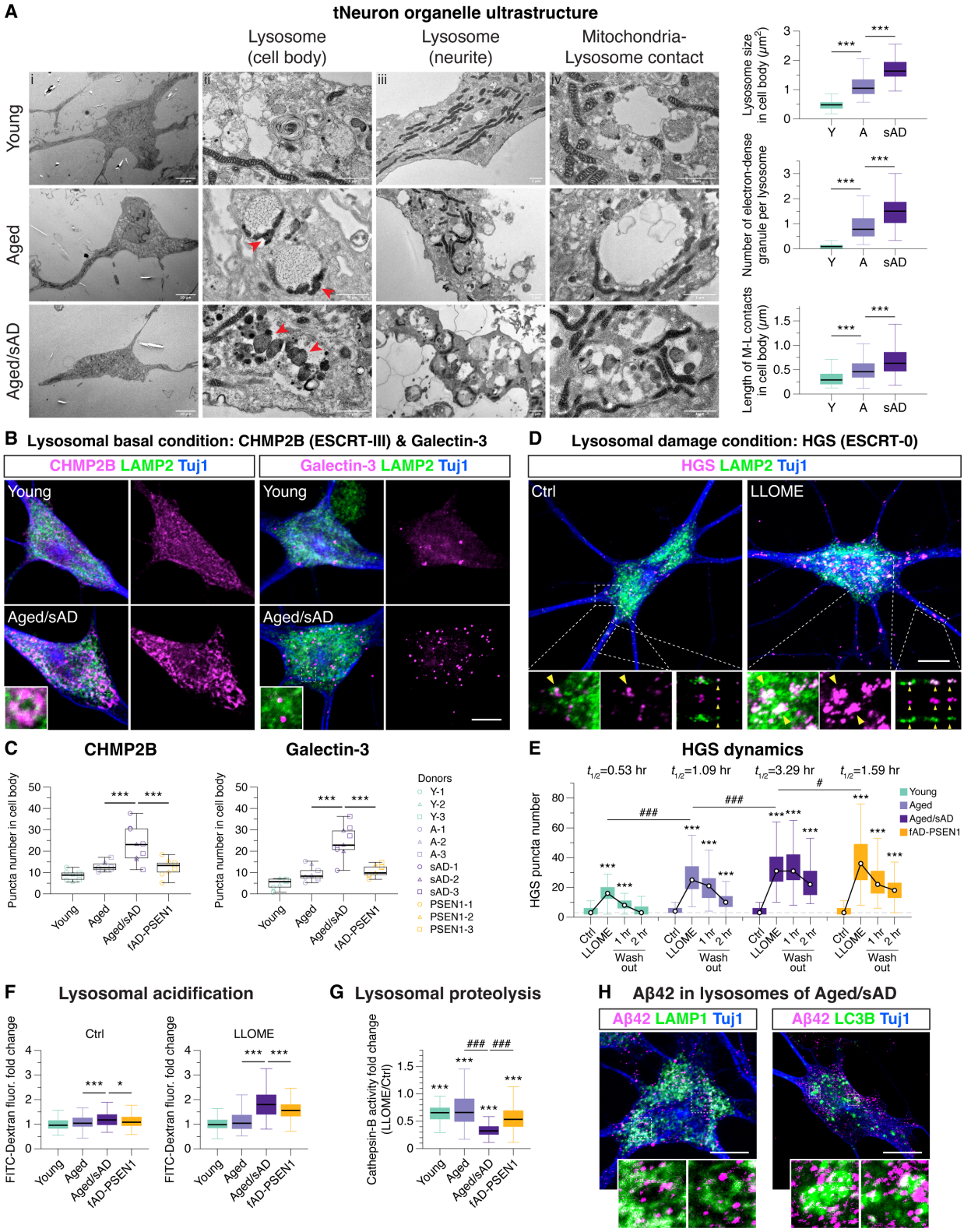

Figure 4 Deficits in lysosomal membrane repair drive lysosomal dysfunction and Aβ pathology in AD tNeurons.

944 (A) TEM for analyzing ultrastructural morphology of lysosomes and mitochondria in human
945 tNeurons. Changes in lysosomal size, electron-dense material abundance and mitochondria-
946 lysosome contacts defined by the contact length are detected in tNeurons. Red arrowhead:
947 electron-dense materials in lysosomes. Scale bar (i): 20 μm. Scale bar (ii-iv): 1 μm.

948 (B) Representative images of tNeurons immunostained for LAMP2 (green), CHMP2B and
949 Galectin-3 (magenta) and Tuj1 (blue) at PID 35. Insert: higher magnification view of CHMP2B
950 and Galectin-3 colocalization with LAMP2. Scale bar: 10 μm.

951 (C) Plots indicate the quantification of numbers of CHMP2B and Galectin-3 puncta in the cell
952 body of tNeurons at the basal condition as shown in panel (B).

953 (D) Representative images of fAD-PSEN1 tNeurons immunostained for LAMP2 (green),
954 ESCRT-0 HGS protein (magenta) and Tuj1 (blue) during 0.25 mM LLOME treatment for 30 min
955 and washout at PID 36. Insert: higher magnification view of HGS and LAMP2 in the cell body
956 and neurites. Yellow arrowhead: HGS colocalization with LAMP2. Scale bar: 10 μm.

957 (E) Plot reflects the lysosomal recovery from damage by measuring the numbers of HGS puncta
958 in the cell body during LLOME treatment and washout as shown in panel (D). The half-life (t1/2)
959 represents the time required for lysosomal recovery in each group.

960 (F) Changes in lysosomal acidification by detecting the intensity of preloaded pH-sensitive
961 FITC-conjugated Dextran in tNeurons at the basal condition and during 0.25 mM LLOME
962 treatment for 30 min.

963 (G) Lysosomal proteolysis reflected by the fold change of Cathepsin-B activity in tNeurons
964 calculated by the value in 0.25 mM LLOME treatment for 30 min relative to the basal condition.

965 (H) Immunofluorescent analysis of colocalization of Aβ42 with LAMP1 and LC3B in aged/sAD
966 tNeurons. Insert: higher magnification view of Aβ42, LAMP1 and LC3B. Scale bar: 10 μm.

967 Data show box-and-whisker plots of 3 independent experiments and 3 cell lines from
968 independent HC and AD donors. Differences between groups are compared with One-Way
969 ANOVA followed by Bonferroni post-hoc analysis. *$P < 0.05$ and ***$P < 0.001$. #$P < 0.05$ and
970 ###$P < 0.001$.

971 See also Figure S5.

972

973

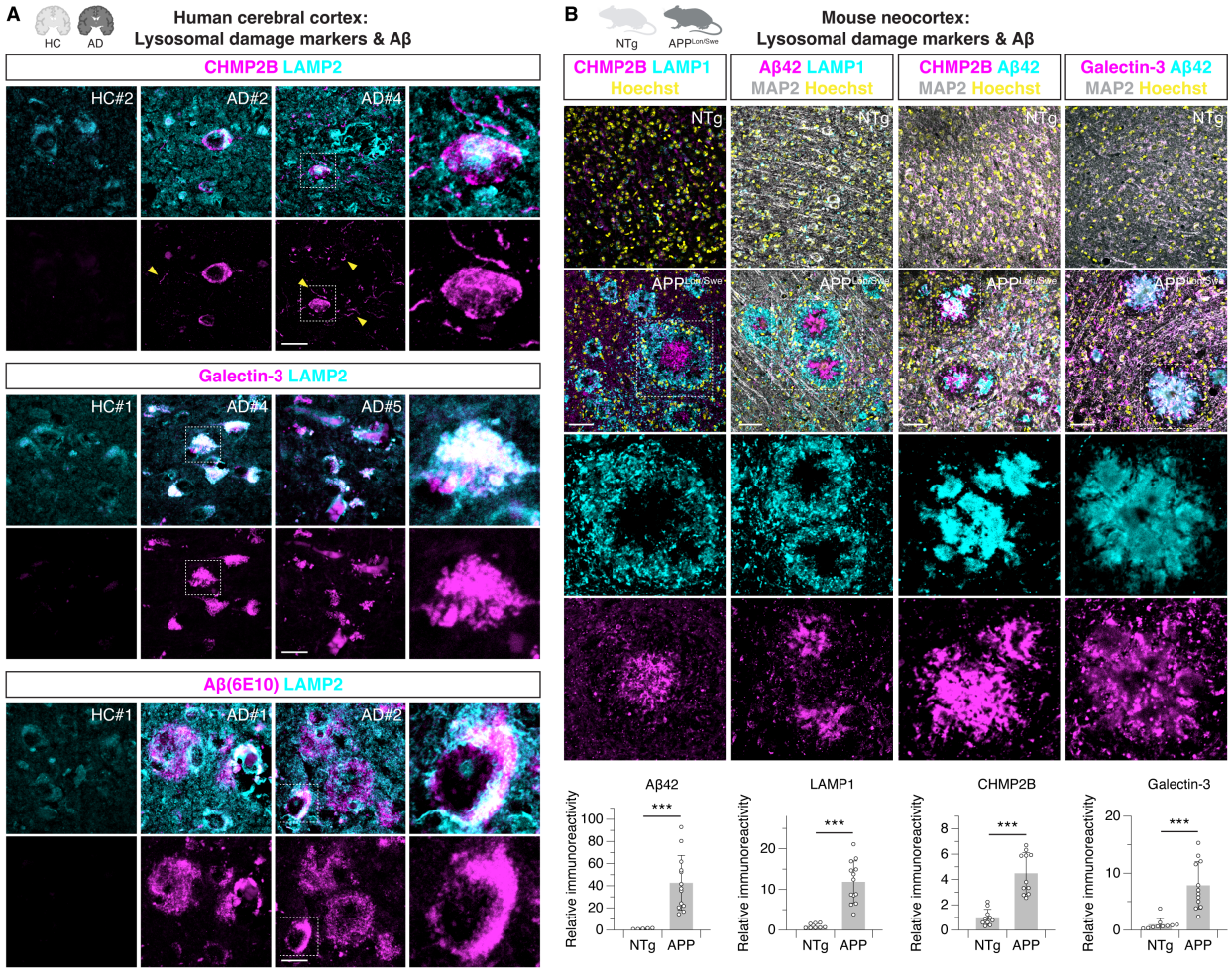

Figure 5 Lysosomal damage is exacerbated in AD and linked to amyloid accumulation in post-mortem brain tissue.

(A) Double immunofluorescent analysis of CHMP2B, Galectin-3 or Aβ (magenta) and LAMP2 (cyan) in the post-mortem cerebral cortex of HC and AD donors. Insert: higher magnification view of CHMP2B, Galectin-3 and Aβ colocalization with LAMP2. Yellow arrowhead: CHMP2B-positive fibril structures. Scale bar: 20 μm.

(B) Immunofluorescent analysis of CHMP2B, Galectin-3, LAMP1 and Aβ42 in the neocortex of non-transgenic wild-type mice (NTg) and transgenic mice expressing mutant human APP with the Swedish (K670N/M671L) and London (V717I) mutations (APPLon/Swe) for modeling AD. The brain tissue is co-stained with MAP2 and Hoechst. Quantitative analysis shows changes in the immunoreactivity of LAMP1, CHMP2B and Galectin-3 in APPLon/Swe mice relative to NTg mice. Insert: higher magnification view of colocalization between CHMP2B, Galectin-3, LAMP1 and Aβ42. Scale bar: 50 μm.

988 Data show mean and SD plots of 3 independent experiments in mice (NTg: n = 8 to 10; APP: n
989 = 10 to 13). Differences between groups are compared with unpaired t test. ***P < 0.001.

990 See also Figures S5 and S6.

991

992

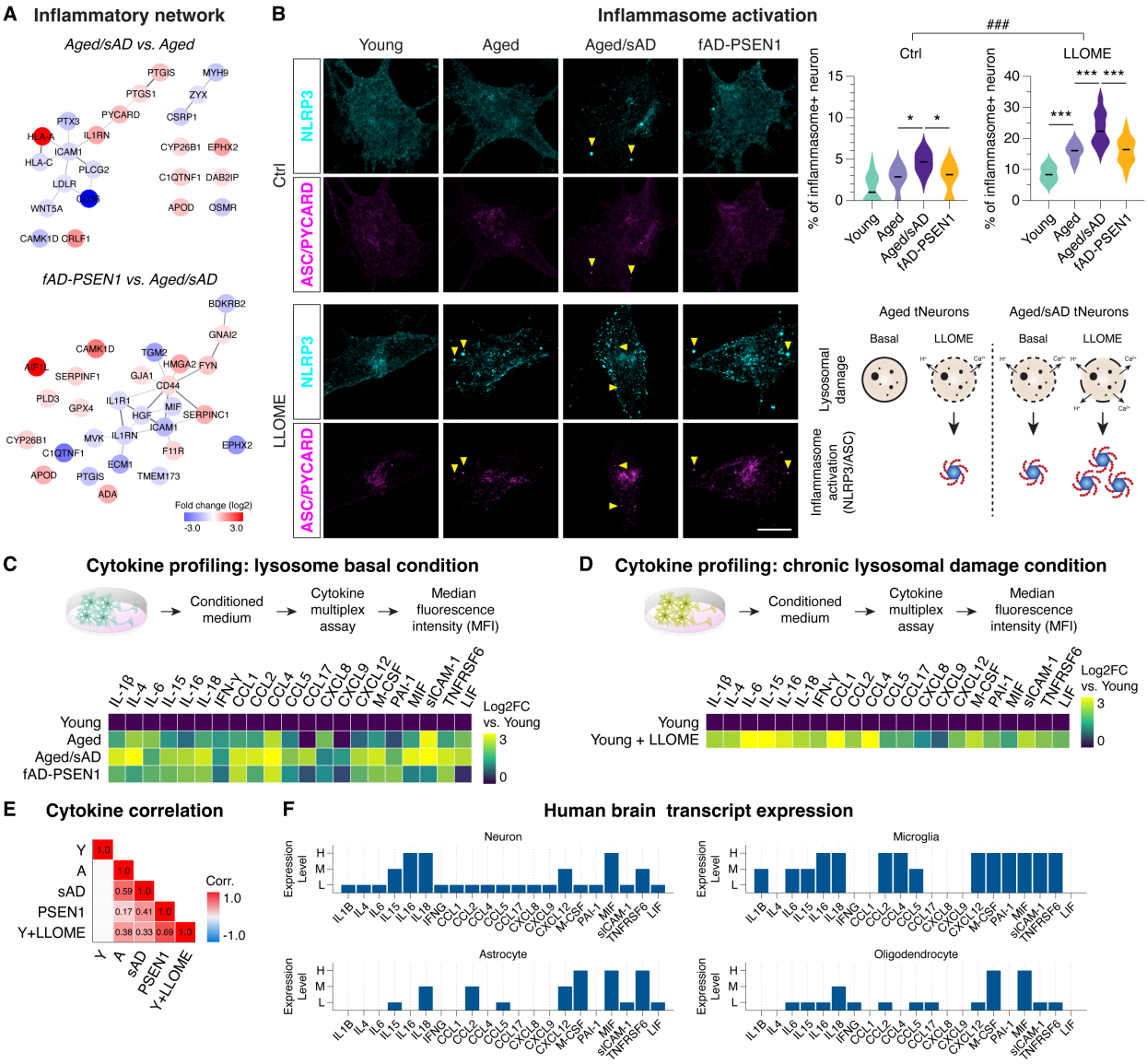

Figure 6 Lysosomal damage mediates inflammatory responses in AD tNeurons.

(A) Proteomic network of tNeuron proteins and the relative abundance in the inflammatory response pathway. The relative abundance indicated by log2-fold change is shown by color: increase in red and decrease in blue.

(B) Representative images of tNeurons immunostained for inflammasome markers NLRP3 (cyan) and ASC (magenta) with or without 0.25 mM LLOME treatment for 3 hr at PID 40. Quantification of the percentage of tNeurons with inflammasomes per image. Schematic for the association between lysosomal vulnerability/damage and inflammasome activation in aged and aged/sAD tNeurons. Yellow arrowhead: colocalization of NLRP3 and ASC. Scale bar: 10 μm.

1003 (C) Experimental schematic for inflammatory profiling of conditioned medium from tNeurons at
1004 the basal condition at PID 40. Heatmap represents the changes in cytokine and chemokine
1005 levels. Exact log2-fold change (Log2FC) and P values can be found in Figure S7A.

1006 (D) Schematic and heatmap for inflammatory profile of conditioned medium from young
1007 tNeurons treated with or without lysosomal damage stress (0.1 mM LLOME starting at PID 33
1008 for 7 days). Exact log2-fold change (Log2FC) and P values can be found in Figure S7A.

1009 (E) Heatmap and Pearson correlation analysis for identified cytokines and chemokines of
1010 tNeurons at the basal and chronic lysosomal damage conditions from panel (C) and (D).
1011 Number in each cell indicates the correlation coefficient.

1012 (F) Single-cell transcriptomic analysis of selected cytokines and chemokines from panel (C) and
1013 (D) in major cell types of human brain, including neuron, astrocyte, microglia and
1014 oligodendrocyte. The transcript expression scores (H: high; M: medium; L: low) is determined by
1015 the expression level of each transcript in public datasets retrieved from the Human Cell Atlas
1016 and Allen Brain Map.

1017 Violin plots depict the median and distributions of data from 3 independent experiments and 3
1018 cell lines from independent healthy controls and AD patients. Inflammatory profiling is
1019 conducted in technical replicates and 2 to 6 cell lines. Log2-fold change in mean fluorescence
1020 intensity (MFI) is compared to the median of young tNeurons. Differences between groups are
1021 compared with One-Way ANOVA followed by Bonferroni post-hoc analysis. *$P < 0.05$ and ***P
1022 < 0.001.

1023 See also Figure S7.

1024

1025

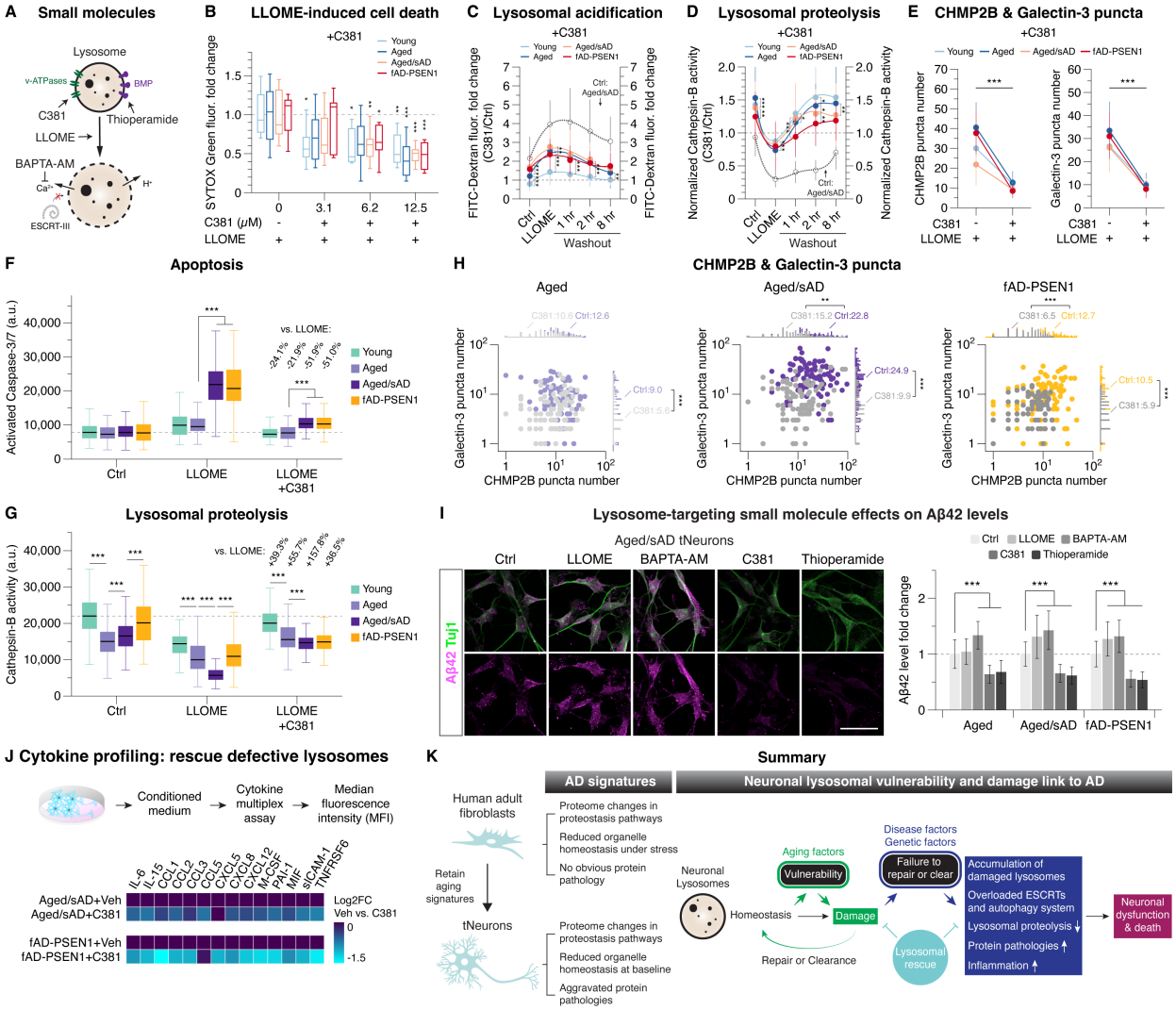

Figure 7 Pharmacological rescue of lysosomal resilience to damage ameliorates AD phenotypes in fibroblasts and tNeurons.

(A) Schematic for small molecules that modulate lysosomal function. C381: regulates lysosomal pH by targeting v-ATPases. Thioperamide: elevates the levels of bis(monoacylglycero)phosphate (BMP). LLOME: triggers lysosomal membrane permeabilization. BAPTA-AM: cell-permeable selective Ca2+ chelator that blocks Ca2+-dependent recruitment of ESCRT-III/Vps4 complex to the damaged lysosome.

(B) Plot profile of a dose-dependent reduction in LLOME-mediated cell death in fibroblasts by C381 pre-treatment for 24 hr. Cells are treated with 1 mM LLOME for 24 hr. The SYTOX intensity is normalized to Hoechst and divided by the value at 0 μM C381 to reflect the fold change by C381.

1038 (C) FITC-dextran intensity is indicative of lysosomal acidity. The pre-treatment of 6.25 μM C381
1039 for 24 hr in fibroblasts is followed by 1 mM LLOME treatment for 30 min and washout (refer to
1040 left y-axis). Dysregulation of lysosomal acidification in aged/sAD fibroblasts (dash line, refer to
1041 right y-axis) shown as a reference control acquired from Figure 4J.

1042 (D) Plot indicates the restoration of lysosomal proteolytic dysfunction in fibroblasts by the pre-
1043 treatment of 6.25 μM C381 for 24 hr. Lysosomal protease Cathepsin-B activity is measured
1044 during LLOME treatment and washout (refer to left y-axis). Defective recovery of Cathepsin-B
1045 activity in aged/sAD fibroblasts (dash line, refer to right y-axis) serving as a reference control
1046 acquired from Figure 4K.

1047 (E) The effect of pre-treatment of 6.25 μM C381 for 24 hr on lysosomal damage in fibroblasts,
1048 indicated by the numbers of CHMP2B and Galectin-3 puncta after 1 mM LLOME treatment for
1049 30 min.

1050 (F) Caspase-3/7 activation, a canonical upstream marker of apoptosis, is found in aged/sAD
1051 and fAD-PSEN1 tNeurons after 0.5 mM LLOME treatment for 1 hr at PID 42. The pre-treatment
1052 of 3.1 μM C381 is continued for 7 days.

1053 (G) Lysosomal proteolysis in tNeurons is reflected by Cathepsin-B activity. The changes in
1054 Cathepsin-B activity can be observed after 0.25 mM LLOME treatment for 30 min at PID 35 or
1055 the pre-treatment of 3.1 μM C381 for 7 days.

1056 (H) 2D Histogram represents the molecular signatures of lysosomal damage by measuring
1057 CHMP2B (x-axis) and Galectin-3 (y-axis) puncta number in aged, aged/sAD and fAD-PSEN1
1058 tNeurons after 0.25 mM LLOME treatment at PID 35. Each dot represents a single neuron and
1059 the number of detectable CHMP2B and Galectin-3 puncta in the cell body. Pre-treatment with
1060 3.1 μM C381 for 7 days alters the CHMP2B and Galectin-3 puncta number.

1061 (I) Lysosomal modulation by small molecules influences the intra-neuronal Aβ42 levels
1062 measured in aged, aged/sAD and fAD-PSEN1 tNeurons. Representative images of aged/sAD
1063 tNeurons immunostained for Aβ42 (magenta) and Tuj1 (green) at PID 35. Quantification of fold-
1064 changes in Aβ42 levels during treatment relative to DMSO control. Scale bar: 50 μm.

1065 (J) Rescue of lysosomal damage reduces the secretion of inflammatory factors from AD
1066 tNeurons. Inflammatory profiling of conditioned medium from aged/sAD and fAD-PSEN1
1067 tNeurons at PID 35 after the treatment of 3.1 μM C381 for 7 days. Exact Log2FC and P values
1068 can be found in Figure S7C.

1069 (K) Summary of aging and AD signatures in fibroblasts and tNeurons, including the aging- and
1070 AD-dependent proteome-wide remodeling and neuron-specific protein pathologies. Proposed
1071 model for the link of lysosomal vulnerability and damage to neurotoxicity in AD and the strategy
1072 for rescuing lysosomal defects in neurons.

1073 Data show box-and-whisker plots of 3 to 6 independent experiments and 3 cell lines from
1074 independent healthy controls and AD patients. Box-and-whisker plots depict 5th, 25th, 50, 75th
1075 and 95th percentiles. Data show mean and SD plots of 3 to 5 independent experiments.
1076 Inflammatory profiling is conducted in technical replicates and 2 cell lines. Differences between
1077 groups are compared with One-Way or Two-Way ANOVA followed by Bonferroni post-hoc
1078 analysis. *$P < 0.05$, **$P < 0.01$ and ***$P < 0.001$.

1079 See also Figure S7.

1080

1081 **STAR Methods**

1082 **Lead Contact for Reagent and Resource Sharing**

1083 Further requests for resources and reagents should be directed to the Lead Contact, Judith
1084 Frydman (jfrydman@stanford.edu).

1085

1086 **Data and Code availability**

1087 All proteomic source data of human fibroblasts and tNeurons have been deposited and are
1088 publicly available at ProteomeXchange (accession number: PXD040834). The mass
1089 spectrometry parameters, sample information, raw data and the comparison between our
1090 datasets and public genomic, transcriptomic and proteomic repositories are provided in Tables
1091 S2 and S4.

1092

1093 **EXPERIMENTAL MODEL AND SUBJECT DETAILS**

1094 **Human subjects**

1095 De-identified human fibroblasts, post-mortem prefrontal cortex and CSF samples were acquired
1096 from individuals of various ages and disease conditions from Stanford Alzheimer's Disease
1097 Research Center (ADRC). Cells and tissue samples were obtained under written consents from
1098 all subjects approved by Institutional Review Board of Stanford University. The cell and tissue
1099 samples collected by ADRC were not specifically for this study. For histological experiments, of
1100 these subjects, 8 were assessed as healthy control (HC) and 10 were patients with cognitive
1101 impairment (dementia due to AD). For CSF proteomics experiments, 50 were assessed as HC
1102 and 29 were patients with cognitive impairment (MCI or dementia due to AD). Age and sex
1103 demographics are detailed in Tables S1 and S3. In the ADRC, all HC and individuals with
1104 cognitive impairment received neurological examinations and cognitive tests to determine
1105 cognitive status and consensus diagnosis by a team of neuropathologists. The pathological
1106 diagnosis of post-mortem tissues was made by microscopic examination of multiple brain
1107 regions using Amyloid score, Braak neurofibrillary degeneration score and CERAD neuritic
1108 plaque score.

1109

1110 **Cell culture**

1111 **HEK293T cells**

1112 The HEK293T cells are the cell line derived human embryonic kidney and were acquired directly
1113 from ATCC (CRL-1573). Cells were grown in culture medium (DMEM supplemented with
1114 GlutaMAX, 10% FBS, 1% Penicillin-Streptomycin, 1% HEPES and 1% Sodium pyruvate)
1115 (ThermoFisher Scientific) sterilized by a 0.22 μm vacuum filter (ThermoFisher Scientific) in a
1116 37°C incubator with 5% CO2 in the air. The HEK293T cells were used for lentiviral production
1117 by transfecting lentiviral vector of interest mixed with packaging and envelope plasmid.
1118 Passaging the cells was performed with Trypsin-EDTA (ThermoFisher Scientific) every three
1119 days.

1120

1121 **Human fibroblasts**

1122 The primary human dermal fibroblasts derived from clinically healthy adults and individuals
1123 diagnosed with AD were collected from the shared resources in the Stanford ADRC and Coriell
1124 Institute for Medical Research, which operates the NIGMS, NIA, NINDS cell repository. Cells
1125 were grown in culture medium (DMEM supplemented with GlutaMAX, 10% FBS, 1% Penicillin-
1126 Streptomycin, 1% MEM NEAA, 1% Sodium pyruvate and 0.1% β-mercaptoethanol)
1127 (ThermoFisher Scientific) sterilized by a 0.22 μm vacuum filter (ThermoFisher Scientific) and
1128 maintained in a 37°C, 5% CO2 incubator. The subculture of proliferating fibroblasts used for
1129 regular experiments and neuronal transdifferentiation was typically within 3 to 7 passages.
1130 Some fibroblast lines obtained with slightly higher passage numbers were used for neuronal
1131 transdifferentiation no more than 12 passages. Passaging the cells was performed with Trypsin-
1132 EDTA every 6-7 days.

1133

1134 **Human tNeurons**

1135 The tNeurons were transdifferentiated from human fibroblasts with low passage numbers using
1136 a combination of transcription factors and small molecules. The method was derived from the
1137 protocols as previously described(Pang et al., 2011; Tanabe et al., 2018). Briefly, the lentiviral
1138 expression of Brn2, Ascl1, Myt1l and Ngn2 in human fibroblasts initiated neuronal
1139 reprogramming. The transduced cells underwent puromycin and PSA-NCAM selection and
1140 cultured in reprogramming medium (DMEM/F12:Neurobasal (1:1) Medium, 2% B-27, 1% N-2,
1141 0.25% GlutaMAX, 1% Penicillin-Streptomycin) (ThermoFisher Scientific) for 15 days and then

1142 switched to maturation medium (BrainPhys Neuronal Medium (STEMCELL Technologies), 2%
1143 B-27, 1% N-2, 0.25% GlutaMAX, 1% Penicillin-Streptomycin) for additional 15 to 22 days. The
1144 culture media were supplemented with BDNF and NT-3 (neurotrophic factors; Peprotech),
1145 Doxycycline (effector for the Tet-On system; Cayman), Forskolin (cAMP activator; Sigma-
1146 Aldrich), SB 431542 (TGF-β/Activin/Nodal inhibitor; TOCRIS), Dorsomorphin (BMP inhibitor;
1147 TOCRIS) and XAV939 (removal from maturation medium) (Wnt inhibitor; Stemgent). The
1148 tNeurons resembled cortical glutamatergic neurons and were used for the evaluation of
1149 reprogramming efficiency, aging and disease signatures, and small molecule treatments after 5
1150 weeks in culture in a 37°C, 5% CO2 incubator. The medium was half-changed every 2-4 days
1151 throughout the lifetime of the culture. Detailed protocol was described in Method Details > Direct
1152 generation of neurons from human fibroblasts.

1153

1154 **Mice**

1155 All mice used in this study were C57BL/6 genetic background. Mice of old age (20-24-month
1156 old) were obtained from the National Institute on Aging rodent colony and young age (3-month
1157 old) were obtained from Jackson Laboratories or Charles River Laboratories. All experiments
1158 used male mice. A transgenic mouse model with the expression of high levels of human
1159 APP751 carrying V717I, K670M/N671L mutations (also referring to APPLon/Swe) in neurons
1160 under control of a Thy1.2 promoter has been studied in different laboratories. The APPLon/Swe
1161 mice developed amyloid plagues associated with an overproduction of Aβ42 in the neocortex
1162 and working memory deficits at 3 months old and the plaque formation spread to the
1163 hippocampus and thalamus region at 5-7 months old(Faizi et al., 2012; Rockenstein et al.,
1164 2001). This study used 3-6-month-old APPLon/Swe and the age-matched non-transgenic mice.
1165 All mice were kept in a 12-hr light/dark cycle in a temperature- and humidity-controlled
1166 environment and provided ad libitum access to food and water. All animal care and procedures
1167 complied with the Animal Welfare Act and were in accordance with institutional guidelines and
1168 approved by the V.A. Palo Alto Committee on Animal Research and the institutional
1169 administrative panel of laboratory animal care at Stanford University.

1170

1171 **METHOD DETAILS**

1172 **Lentivirus preparation**

1173 The FUW lentiviral vector expressing single transcription factor, including Brn2, Ascl1, Myt1l,
1174 and Ngn2-puro (also referring as BAMN factors), or EGFP is under the control of TetO promoter
1175 and M2rtTA under the control of ubiquitin promoter. The HEK293T cells (ATCC) were plated at
1176 a density of 6 x 106 in a poly-L-ornithine-coated 10-cm dish and the next day co-transfected
1177 with 5 µg lentiviral transfer vector, 4 µg packaging plasmid (psPAX2) and 2.5 µg envelope
1178 plasmid (pMD2.G) using Lipofectamine 2000 in OptiMEM (ThermoFisher Scientific). After 6-hr
1179 incubation of Lipofectamine/DNA mixture in OptiMEM, the transfection medium was replaced
1180 with fresh DMEM supplemented with GlutaMAX, 2% FBS, 1% Penicillin-Streptomycin, 1%
1181 HEPES and 0.1% BME (ThermoFisher Scientific). The cell supernatants containing lentiviral
1182 particles were harvested after 24 hr and stored at 4°C. Cells were replenished with fresh DMEM
1183 medium with 2% FBS and cultured for additional 24 hr. The supernatants were then harvested
1184 and pooled with the first collection. To remove cell debris, the supernatants were centrifugated
1185 at 400 x G for 5 min and passed through 0.45 µm syringe filters. The clear virus-containing
1186 media can be stored at 4°C for about 1 week. For long-term storage, alternatively, the virus-
1187 containing media were spun by ultracentrifugation at 25,000 rpm for 90 min at 4°C to pellet the
1188 viruses. The viruses were resuspended in DMEM medium with 2% FBS and snap-frozen in
1189 small aliquots to store at -80°C.

1190

1191 **Direct generation of neurons from human fibroblasts**

1192 Human adult fibroblasts were plated at a density of 200 × 103 per well of a 6-well plate coated
1193 with poly-L-ornithine. The next day, fibroblasts were infected with lentiviruses expressing BAMN
1194 factors and M2rtTA with or without EGFP by incubating with the diluted virus-containing medium
1195 in DMEM supplemented with GlutaMAX, 2% FBS, 1% Penicillin-Streptomycin, 1% HEPES and
1196 0.1% BME plus 4 µg/mL Polybrene for 24 hr. The virus-containing medium was then discarded
1197 and replaced by fresh fibroblast culture medium plus 1 µg/mL Doxycycline, followed by
1198 puromycin (0.5 µg/mL) selection for 48 hr. The transduced cells were subjected to PSA-NCAM+
1199 selection following the manufacturer's instructions. Briefly, 0.05% Trypsin-EDTA was added to
1200 the cells for 5 min at 37°C to dissociate the cells from surface and neutralized by fibroblasts
1201 culture medium, followed by the centrifugation at 300 x G for 5 min at room temperature to pellet
1202 cells. The cells were resuspended in autoMACS buffer and labeled with anti-PSA-NCAM-APC
1203 (Miltenyi Biotec) for 10 min at 4°C in the dark. After a wash by autoMACS buffer and
1204 centrifugation at 300 x G for 10 min, the cells were incubated with anti-APC MicroBeads
1205 (Miltenyi Biotec) for 15 min at 4°C in the dark. Unbound beads were then washed off and the

1206 cells were resuspended in autoMACS buffer for subsequent flow cytometry analysis and
1207 separation of magnetically PSA-NCAM-labeled and unlabeled cells. The PSA-NCAM+ cells
1208 were re-plated at a density of 50 × 103 cells per cm2 to the plate coated with vitronectin (VTN-
1209 N, 5 µg/mL; ThermoFisher Scientific) and laminin (rhLaminin-521, 1 µg/mL; Corning). Cells were
1210 cultured in the fibroblast culture medium plus 1 µg/mL Doxycycline and the next day switched to
1211 the reprogramming medium (DMEM/F12:Neurobasal (1:1) Medium, 2% B-27, 1% N-2, 0.25%
1212 GlutaMAX, 1% Penicillin-Streptomycin) (ThermoFisher Scientific) supplemented with small
1213 molecules: 1 µg/mL Doxycycline (Cayman), 5 µM Forskolin (Sigma-Aldrich), 10 µM SB 431542
1214 (TOCRIS), 2 µM Dorsomorphin (TOCRIS) and 2 µM XAV939 (Stemgent). After one week, 10
1215 ng/mL BDNF and NT-3 (Peprotech) were added to the reprogramming medium. Half of the
1216 medium was changed every 2 to 3 days. After 8 days, cells were switched to maturation
1217 medium (BrainPhys Neuronal Medium (STEMCELL Technologies), 2% B-27, 1% N-2, 0.25%
1218 GlutaMAX, 1% Penicillin-Streptomycin) supplemented with 1 µg/mL Doxycycline, 5 µM
1219 Forskolin, 10 µM SB 431542, 2 µM Dorsomorphin and 10 ng/mL BDNF and NT-3 and cultured
1220 for additional 15 to 22 days. Half of the medium was changed every 3 to 4 days. The efficiency
1221 of transdifferentiation of human fibroblasts into tNeurons was measured by the percentage of
1222 remaining transduced cells that express Tuj1, NeuN and MAP2 and the percentage of EGFP-
1223 positive cells showing neuron-like morphology.

1224

1225 **Quantitative proteomics (TMT, Tandem Mass Tag)**

1226 Flash frozen cell pellets were lysed in 8M urea buffer (8M urea, 150 mM NaCl, 50 mM HEPES
1227 pH 7.5, 1x EDTA-free protease inhibitor cocktail (Roche), 1x PhosSTOP phosphatase inhibitor
1228 cocktail (Roche)). Lysates were clarified by centrifugation at 17,000 x g for 15 min at 4°C.
1229 Protein concentration of the supernatant was quantified by bicinchroninic acid assay (BCA,
1230 Pierce). To reduce and alkylate cysteines, 100 µg of protein was sequentially incubated with 5
1231 mM TCEP for 30 min, 14 mM iodoacetamide for 30 min, and 10 mM DTT for 15 min. All
1232 reactions were performed at room temperature. Next, proteins were chloroform-methanol
1233 precipitated and the pellet resuspended in 200 mM EPPS pH 8.5. Then, LysC (Wako) was
1234 added at 1:100 (LysC:protein) ratio and incubated overnight at room temperature in an orbital
1235 shaker at 1,500 rpm. The day after, samples were further digested for 5 hr at 37ºC with trypsin
1236 at 1:75 (trypsin:protein) ratio in an orbital shaker at 1,500 rpm. After digestion, samples were
1237 clarified by centrifugation at 17,000 x g for 10 min. Peptide concentration of the supernatant was
1238 quantified using a quantitative colorimetric peptide assay (ThermoFisher). For TMT labelling we

1239 used 2 different kits to label each of the TMT experiments included in this manuscript. In TMT-
1240 01, peptides from fibroblast's samples were labelled with TMT-6plex tags. In TMT-02, peptides
1241 from tNeuron's samples were labelled with TMTpro-16plex tags. Same method was followed to
1242 label both TMT sets(Cao et al., 2021a; Liu et al., 2022; Nguyen et al., 2017). Briefly, 25 □g of
1243 peptides was brought to 1 µg/µl with 200 mM EPPS (pH 8.5), acetonitrile (ACN) was added to a
1244 final concentration of 30% followed by the addition of 50 µg of each TMT reagents. After 1 hr of
1245 incubation at room temperature, the reaction was stopped by the addition of 0.3%
1246 hydroxylamine (Sigma) for 15 min at room temperature. Extra information regarding both TMT
1247 sample labels is included in Table S4. After labelling, samples of each TMT were combined,
1248 desalted with tC18 SepPak solid-phase extraction cartridges (Waters), and dried in the
1249 SpeedVac. Next, desalted peptides were resuspended in 5% ACN, 10 mM NH4HCO3 pH 8.
1250 Both TMT were fractionated in a basic pH reversed phase chromatography using a HPLC
1251 equipped with a 3.5 µm Zorbax 300 Extended-C18 column (Agilent). Fractions were collected in
1252 a 96-well plate, then combined into 24 samples. Twelve of them were desalted following the
1253 C18 Stop and Go Extraction Tip (STAGE-Tip)(Rappsilber et al., 2003) and dried down in a
1254 SpeedVac. Finally, peptides were resuspended in 1% formic acid, 3% ACN, and analyzed by
1255 LC-MS3 in an Orbitrap Fusion Lumos (ThermoFisher). For TMT-01 the MS was running in SPS-
1256 MS3 mode(McAlister et al., 2014). For TMT-02, instrument was equipped with FAIMS and
1257 running in RTS-MS3 mode(Schweppe et al., 2020a; Schweppe et al., 2019; Schweppe et al.,
1258 2020b). More information regarding all MS parameters used for both TMT are included in Table
1259 S4. A suite of in-house pipeline (GFY-Core Version 3.8, Harvard University) was used to obtain
1260 final protein quantifications from all RAW files collected. RAW data were converted to mzXML
1261 format using a modified version of RawFileReader (5.0.7) and searched using the search
1262 engine Sequest or Comet (for TMT-01 and TM-02 respectively)(Eng et al., 2008; Eng et al.,
1263 2013; Eng et al., 1994) against a mouse target-decoy protein database (downloaded from
1264 UniProt in June 2019) that included the most common contaminants. Precursor ion tolerance
1265 was set at 20 ppm and product ion tolerance at 1 Da. Cysteine carbamidomethylation (+57.0215
1266 Da) and TMT tag (+229.1629 Da or +304.2071 Da for TMT-6plex or TMTpro-16pex,
1267 respectively) on lysine residues and peptide N-termini were set as static modifications. Up to 2
1268 variable methionine oxidations (+15.9949 Da) and 2 miss cleavages were allowed in the
1269 searches. Peptide-spectrum matches (PSMs) were adjusted to a 1% FDR with a linear
1270 discriminant analysis(Huttlin et al., 2010) and proteins were further collapsed to a final protein-
1271 level FDR of 1%. TMT quantitative values we obtained from MS3 scans. Only those with a
1272 signal-to-noise ratio > 100 and an isolation specificity > 0.7 were used for quantification. Each

1273 TMT was normalized to the total signal in each column. Quantifications included in Table S4 are
1274 represented as relative abundances. RAW files will be made available upon request. The data
1275 have been deposited in the ProteomeXchange Consortium via the PRIDE(Vizcaíno et al., 2014)
1276 partner repository with the data set identifier PXD040834. Biological pathway and gene ontology
1277 enrichment analysis were performed using the ClueGo (Cytoscape plug-in), Enrichr or STRING.

1278

1279 **SYTOX Green assay for measuring cell death**

1280 The nucleic acid dye SYTOX Green (ThermoFisher Scientific) was diluted to 100 μM in DMSO
1281 and stored at -20°C. Human fibroblasts were seeded at 5 x 103 per well of a 96-well plate
1282 treated with DMSO or LLOME at a series of concentrations to evaluate the lysosome-mediated
1283 cell death or pre-treated with C381 followed by 2 mM LLOME to evaluate the rescue of
1284 lysosome-mediated cell death. The uptake of membrane-impermeant SYTOX Green dye occurs
1285 while cell membrane is compromised. The fluorescent nucleic acid-intercalating dyes then emit
1286 a significant increase in fluorescence intensity as dead-cell markers. SYTOX Green staining
1287 solution was prepared at a final concentration of 100 nM in HBSS and incubated with cells for
1288 30 min at 37°C. After rinse once with PBS, cells were monitored for SYTOX Green intensity
1289 changes in CLARIOstar plate reader. Then, the cells were rinsed once with PBS, counterstained
1290 with 5 μg/mL Hoechst (ThermoFisher Scientific) for 10 min at room temperature and rinsed with
1291 PBS. The measurement of Hoechst fluorescence is performed in plate reader and allowed
1292 SYTOX Green levels to be normalized to the cell density.

1293

1294 **Caspase-3/7 activation**

1295 To detect neuronal apoptosis, we added the Caspase-3/7 substrate FAM-DEVD-FMK
1296 (ImmunoChemistry), one of the fluorochrome-labeled inhibitors of caspases that covalently and
1297 irreversibly binds to the active caspases. The green fluorescence intensity is a direct
1298 measurement of Caspase-3/7 activity. Human tNeurons were treated with DMSO or 0.5 mM
1299 LLOME for 1 hr to measure the lysosome-mediated apoptosis or pretreated with 3.1 μM C381
1300 followed by LLOME treatment to assess the rescuing effect on lysosome-mediated apoptosis.
1301 The FAM-DEVD-FMK reagent was reconstituted in DMSO and stored at -20°C. When cells
1302 were available, the FAM-DEVD-FMK reagent was diluted with PBS 1:5 ratio and added to cell
1303 culture medium at a dilution of 1:30 to form 1X staining solution. Cells were incubated with the
1304 FAM-DEVD-FMK solution for 30 min at 37°C. After a rinse by Apoptosis Buffer, the cells were

1305 fixed by 4% PFA for 15 min and counterstained with 5 μg/mL Hoechst for confocal microscope
1306 imaging.

1307

1308 **Lysotracker**

1309 LysoTracker Red DND-99 was reconstituted in DMSO and stored at -20°C. Human adult
1310 fibroblasts were seeded at 5 x 103 per well of a 96-well plate and pre-incubated with 0.1 μM
1311 LysoTracker Red for 30 min at 37°C. After washing off excess dye by PBS, cells were treated
1312 with 1 mM LLOME for up to 60 min to evaluate the lysosomal activity. After a wash by PBS,
1313 cells were prepared for imaging by CLARIOstar plate reader.

1314

1315 **Fluorescence-conjugated Dextran assay for measuring endocytosis and lysosomal**
1316 **acidification**

1317 Fluorescein isothiocyanate (FITC)-conjugated Dextran at 40 kDa and tetramethylrhodamine
1318 (TMR)-conjugated Dextran at 70 kDa (ThermoFisher Scientific) were reconstituted in H2O and
1319 stored at -20°C. Human adult fibroblasts were seeded at 4 x 104 per well of a 24-well plate or 5
1320 x 103 per well of a 96-well plate. Cells were incubated with FITC- and TMR-Dextran at 0.5
1321 mg/ml for 4 hr at 37°C and rinsed by PBS, followed by 20-hr chase in fresh culture medium to
1322 accumulate Dextran in the late endosomes and lysosomes. Then, cells were treated with DMSO
1323 or 1 mM LLOME for 30 min and washed out to assess the cellular endocytosis and lysosomal
1324 recovery function, or pre-treated with 6.25 μM C381 for 24 hr, followed by LLOME treatment and
1325 washout to evaluate the rescuing effect of C381 in fibroblasts. The cells were fixed by 4%
1326 paraformaldehyde (PFA) for 15 min and prepared for imaging by a confocal microscope and
1327 CLARIOstar plate reader.

1328

1329 **Magic Red Cathepsin-B assay for measuring lysosomal proteolysis**

1330 Magic Red Cathepsin-B substrate, MR-(RR)2, containing arginine-arginine (RR) sequence was
1331 reconstituted in DMSO and stored at -20°C. When cells were available for experiment, MR-
1332 (RR)2 was diluted with H2O 1:10 ratio and added to cell culture medium at a dilution of 1:25 to
1333 form 1X staining solution. Active Cathepsin-B cleaves MR-(RR)2 and emits fluorescence with
1334 optimal excitation of 592 nm and emission of 628 nm. To test lysosomal proteolytic capacity,
1335 human adult fibroblasts were incubated MR-(RR)2 staining solution with for 30 min at 37°C,

1336 followed by DMSO or 1 mM LLOME treatment for 30 min and washout for lysosomal recovery
1337 experiment. To evaluate the pharmacological rescuing effect, the C381 treatment was 24 hr
1338 before the cells were loaded with MR-(RR)2. Cells were treated with 1 mM LLOME for 30 min
1339 and washed out, and then fixed by 4% PFA for 15 min for imaging by a confocal microscope
1340 and CLARIOstar plate reader.

1341

1342 **Mice brain perfusion and tissue processing**

1343 Mice were anaesthetized with 2.5% (v/v) Avertin (Sigma-Aldrich). Transcardial perfusion with
1344 50 ml cold PBS was performed using a peristaltic pump with the perfusate flow rate not
1345 exceeding 10 ml/min. Brain tissue processing was performed as described previously(Vest et
1346 al., 2022; Villeda et al., 2014). Hemibrains were isolated and fixed in 4% PFA overnight at 4°C
1347 before transferring to 30% sucrose in PBS at 4 °C for preservation. Hemibrains were
1348 cryosectioned coronally at a thickness of 40 µm on a freezing–sliding microtome, and the free-
1349 floating sections were stored in cryoprotectant (40% PBS, 30% glycerol, 30% ethylene glycol)
1350 and kept at -20 °C until staining.

1351

1352 **Immunofluorescence and image acquisition and analysis**

1353 Human adult fibroblasts were fixed with 4% PFA for 15 minutes at room temperature,
1354 permeabilized with 0.3% Triton X-100 in PBS for 5 minutes or cold Methanol on ice for 20
1355 minutes, blocked with pre-warmed 5% bovine serum albumin (BSA) in PBS and shook for 45
1356 min at room temperature. Fibroblasts were incubated with primary antibody solution in 5% BSA
1357 overnight at 4°C in a moisture chamber: anti-ALIX (1:200; Santa Cruz, sc-53540), anti-Amyloid-
1358 β (1:100; Cell Signaling, 8243), anti-Amyloid-β (1-42) (1:200; Enzo Life Sciences, ADI-905-804-
1359 100), anti-CHMP1A (1:200; Santa Cruz, sc-271617), anti-CHMP2B (1:400; Proteintech, 12527-
1360 1-AP), anti-CHMP6 (1:200; Santa Cruz, sc-398963), anti-Galectin-3 (1:1000; Biolegend,
1361 125401), anti-γ-H2AX (1:200; Millipore Sigma, 05-636), anti-H3K9me3 (1:500; Abcam, ab8898),
1362 anti-H4K16ac (1:300; Thermo Fisher Scientific, MA5-27794), anti-Hsp70 (1:1000; Abcam,
1363 ab45133), anti-LAMP1 (1:2000; Cell Signaling, 9091), anti-LAMP2 (1:200; DSHB, H4B4), anti-
1364 LC3B (1:200; Cell Signaling, 2775)., anti-Nup98 (1:500; Cell Signaling, 2598), anti-
1365 p62/SQSTM1 (1:400; Abcam, ab56416), anti- S100A4 (1:200; Abcam, ab124805), anti-TDP-43
1366 (1:1000; Proteintech, 12892-1-AP), anti-TFEB (1:100; Proteintech, 13372-1-AP), anti-TSG101
1367 (1:200; Santa Cruz, sc-7964), anti-Ubiquitin (1:200; LifeSensors, AB120), and anti-Vimentin

1368 (1:400; Cell Signaling, 5741). Fibroblasts were washed with PBS three times and incubated with
1369 fluorophore-conjugated secondary antibody solution in the dark for 1 hr at room temperature:
1370 anti-mouse, anti-rabbit and anti-rat (1:500, Thermo Fisher Scientific). Finally, fibroblasts were
1371 washed with PBS three times, mounted with DAPI containing ProLong Glass Antifade Mountant
1372 (Thermo Fisher Scientific) and air-dried for overnight prior to imaging.

1373

1374 Human tNeurons were undergone two-step fixation: 1) remove half the culture medium and add
1375 equivalent to half the volume of 4% PFA for 5 min at room temperature; 2) remove the old
1376 solution and add 4% PFA for 15 min at room temperature. The tNeurons were permeabilized
1377 with 0.3% Triton X-100 in PBS for 5 minutes at room temperature or cold Methanol on ice for 20
1378 minutes, blocked with pre-warmed 5% bovine serum albumin (BSA) in PBS and shook for 45
1379 min at room temperature. Fibroblasts were incubated with primary antibody solution in 5% BSA
1380 overnight at 4°C in a moisture chamber: anti-ASC/PYCARD (1:100; Santa Cruz, sc-514414),
1381 anti-GAP-43 (1:300; Novus Biologicals, NB300-143), anti-HGS (1:200; Genetex, GTX101718),
1382 anti-MAP2 (1:1000; Biolegend, 822501), anti-NeuN (1:500; Abcam, ab177487), anti-NLRP3
1383 (1:200; R&D systems, MAB7578), anti-pTau (AT8) (1:100; Thermo Fisher Scientific, MN1020),
1384 anti-pTDP-43 Ser409/410 (1:300; Cosmo Bio, CAC-TIP-PTD-M01), anti-Synapsin-1 (Syn-1)
1385 (1:200; Abcam, ab64581), anti-Tau (1:100; Aves Labs), and anti-Beta tubulin III (Tuj1) (1:500;
1386 Neuromics, CH23005 & 1:1000; Biolegend, 801201). The tNeurons were washed with PBS
1387 three times and incubated with fluorophore-conjugated secondary antibody solution in the dark
1388 for 1 hr at room temperature: anti-mouse, anti-rabbit and anti-rat, and anti-chicken (1:500,
1389 Thermo Fisher Scientific), washed with PBS three times, mounted with DAPI containing
1390 ProLong Glass Antifade Mountant (Thermo Fisher Scientific) and air-dried for overnight prior to
1391 imaging.

1392

1393 Free-floating mouse tissue sections at 30-50 μm were collected and proceed for
1394 immunostaining in multi-well plates. Mouse tissue sections were first rinsed with PBS three
1395 times and permeabilized with 0.3% Triton X-100 in PBS for 20 min at room temperature,
1396 followed by incubation with blocking buffer (10% Normal Donkey Serum and 0.03% Triton-X-
1397 100 in PBS) and shook for 1 hr at room temperature. After PBS rinsing, the tissue sections were
1398 incubated with primary antibody solution in 10% Normal Donkey Serum in PBS overnight at 4°C
1399 in a moisture chamber: anti-Amyloid-β (1-42) (1:100; Enzo Life Sciences, ADI-905-804-100),

1400 anti-CHMP2B (1:100; Proteintech, 12527-1-AP), anti-Galectin-3 (1:50; R&D systems, AF1197),
1401 anti-Hsp70 (1:300; Abcam, ab45133), anti-LAMP1 (1:50; Santa Cruz, sc-19992), and anti-MAP2
1402 (1:500; Biolegend, 822501). Fluorophore-conjugated secondary antibody solution was
1403 incubated for 1 hr at room temperature: anti-mouse, anti-rabbit, anti-goat and anti-chicken
1404 (1:500, Thermo Fisher Scientific). Tissue sections were washed with PBS two times,
1405 counterstained with Hoechst (1:2000) and washed with PBS two times again before mounting
1406 with ProLong Glass Antifade Mountant (Thermo Fisher Scientific). Samples were air-dried for
1407 overnight prior to imaging.

1408

1409 Paraffin-embedded human brain tissues of the cerebral cortex were sectioned at 10 μm
1410 thickness. Deparaffinization was achieved by washing slides through xylenes twice, each for 5
1411 min and rehydrating via gradient ethanol (100% □ 95% □ 70% □ 50%) into water, each for 10
1412 min. Following heat-mediated antigen retrieval using Citrate buffer, pH 6.0 (Sigma-Aldrich) for
1413 30 min at 95° C, tissue sections were rinsed with PBS once and incubated with blocking buffer
1414 (10% Normal Donkey Serum and 0.03% Triton-X-100 in PBS) for 2 hr at room temperature.
1415 Slides were incubated with antibody cocktails in blocking buffer overnight at 4°C in a moisture
1416 chamber: Amyloid-β (6E10) (1:100; Biolegend, 803001), anti-CHMP2B (1:100; GeneTex,
1417 GTX118181), anti-Galectin-3 (1:50; R&D systems, AF1197 & 1:100; Biolegend, 125401), anti-
1418 Hsp70 (1:300; Abcam, ab45133), anti-LAMP2 (1:200; Abcam, ab213294), and anti-MAP2
1419 (1:500; Biolegend, 822501). Tissue sections were incubated with fluorophore-conjugated
1420 secondary antibody solution for 1 hr at room temperature: anti-mouse, anti-rabbit, anti-rat, anti-
1421 goat and anti-chicken (1:500, Thermo Fisher Scientific). After a PBS rinse, slides were
1422 counterstained with Hoechst (1:2000) and washed with PBS two times. The complete air-dried
1423 tissue sections were mounted with ProLong Glass Antifade Mountant (Thermo Fisher Scientific)
1424 and subjected to dry in the dark overnight prior to imaging.

1425

1426 Imaging was acquired at Z-series (10-30 sections, 0.2-1 μm steps) according to experimental
1427 paradigm using Zeiss LSM 700 confocal fluorescence microscope with 20x, 63x and 100x
1428 objectives. In each experiment, all groups were subjected to image using the same acquisition
1429 settings. The z-stack images were performed Maximum Intensity Projection to analyze the
1430 mean pixel intensity and determine a threshold to quantify puncta number in the cells by Fiji. For
1431 quantitative histology, three to five separate sections were sampled using a 20x objective and

1432 fluorescence signals were measured from entire image field to the mean fluorescence change.
1433 Tissue sections were imaged and analyzed by blinded observers.

1434

1435 **Transmission electron microscopy**

1436 Cells were grown on Ibidi dishes: μ-Dish 35 mm, high Grid-50 Glass Bottom is a 35 mm then
1437 fixed in Karnovsky's fixative: 2% Glutaraldehyde (EMS Cat# 16000) and 4% pFormaldehyde
1438 (EMS Cat# 15700) in 0.1M Sodium Cacodylate (EMS Cat# 12300) pH 7.4 for 1 hr, chilled and
1439 sent to Stanford's CSIF on ice. They were then post-fixed in cold 1% Osmium tetroxide (EMS
1440 Cat# 19100) in water and allowed to warm for 2 hr in a hood, washed 3X with ultra-filtered
1441 water, then en bloc stained 2 hr in 1% Uranyl Acetate at room temperature. Samples were then
1442 dehydrated in a series of ethanol washes for 10 min each at room temperature beginning at
1443 30%, 50%, 70%, 95%, changed to 100% 2X, then Propylene Oxide (PO) for 10 min. Samples
1444 were infiltrated with EMbed-812 resin (EMS Cat#14120) mixed 1:1, and 2:1 with PO for 2 hr
1445 each. The samples were then placed into EMbed-812 for 2 hours opened then placed into flat
1446 molds w/labels and fresh resin and placed into 65o C oven overnight. Cells of interest were
1447 located using the grid pattern and cut out with a gem saw and remounted on pre-labeled resin
1448 blocks with fresh resin and polymerized overnight again. Once full polymerized the glass
1449 coverslip was etched away using hydrofluoric acid for 20 min. Using the finder grid pattern left
1450 behind the block faces were trimmed down allowing for serial sectioning of the cells of interest.
1451 Sections were taken around 90 nm, picked up on formvar/Carbon coated slot Cu grids, stained
1452 for 40seconds in 3.5% Uranyl Acetate in 50% Acetone followed by staining in 0.2% Lead Citrate
1453 for 6 min. Observed in the JEOL JEM-1400 120kV and photos were taken using a Gatan Orius
1454 2k X 2k digital camera.

1455

1456 **Cytokine profiling analysis on neuronal conditioned medium using Luminex multiplex**
1457 **analysis**

1458 Secretion of inflammatory factors was analyzed using cytokine profiling of the conditioned
1459 medium from tNeurons of healthy donors and AD patients. Conditioned medium was collected
1460 48 hr after the last medium change in a 12-well plate with 1 mL of neuronal maturation medium
1461 at PID 38, and centrifuged at 10,000 x G for 10 min at room temperature to pellet out
1462 particulates. For Human 80 plex panel (EMD-Millipore), a minimum of 200 μL of supernatants
1463 was stored at -80°C. Cell free medium was also collected to monitor the background

1464 fluorescence. Cell numbers were determined by an automated cell counter for normalization of
1465 cytokine levels. The setup of cytokine profiling assay was performed according to the
1466 manufacturer's instructions. Briefly, samples were mixed with antibody-linked magnetic beads
1467 on a 96-well plate and incubated overnight at 4°C with shaking. Cold and room temperature
1468 incubation steps were performed on an orbital shaker at 500-600 rpm. Plates were washed
1469 twice with wash buffer in a Biotek ELx405 washer. Following one hr incubation at room
1470 temperature with biotinylated detection antibody, streptavidin-PE was added for 30 minutes with
1471 shaking. Plates were washed as above and PBS added to wells for reading in the Luminex
1472 FlexMap3D Instrument with a lower bound of 50 beads per sample per cytokine. Each sample
1473 was measured in duplicate. Custom Assay Chex control beads were purchased from Radix
1474 Biosolutions, Georgetown, Texas, and are added to all wells. The analyses of all conditioned
1475 medium samples were performed using raw data (mean fluorescence intensity (MFI)) rather
1476 than concentration (pg/mL) to avoid calculating bias per as per recommendation of the Stanford
1477 Human Immune Monitoring Center.

1478

1479 **CSF samples and protein discovery**

1480 We used the SOMAScan assay platform(Gold et al., 2010; Kim et al., 2018a) (SomaLogic Inc.)
1481 to measure the relative levels of 76 human proteins in CSF. This platform is based on modified
1482 single-stranded DNA aptamers (SOMAmer) capable of binding to specific protein targets with
1483 high sensitivity and specificity. We collected 79 CSF samples (50 HC and 29 AD samples) from
1484 a multi-ethnic cohort of older American adults (age range 60-87 years) between 2015 and 2020.
1485 Samples were stored at -80 °C and 150 µl aliquots of CSF were sent on dry ice to SomaLogic.
1486 CSF samples were analyzed via SOMAScan assay in five batches. To account for variation
1487 within and across batches, control, calibrator and buffer samples are added in each 96-well
1488 plate. Data normalization was conducted by the manufacturer following three stages. First, in
1489 Hybridization Control Normalization, hybridization control probes are used to remove individual
1490 sample variance. Second, Intraplate Median Signal Normalization, median normalization
1491 removed inter-sample differences within the plate. Last, Plate Scaling and Calibration, this final
1492 step removed variance across assay runs.

1493

1494 **QUANTIFICATION AND STATISTICAL ANALYSIS**

1495 Quantification of fluorescence images was performed by CLARIOstar plate reader software and
1496 open-source Fiji software. For each technical replicate, the fluorescence intensity of the
1497 background from cell-free solution or cell-free area in the image field was subtracted from
1498 intensity measurements. For most experiments, a power analysis was performed to pre-
1499 determine the sample sizes based on results from initial experiments. For quantifications of
1500 cytokine levels and human and mouse brain samples, the experiments were blinded. Statistical
1501 analysis was performed with unpaired t-test, one- way ANOVA or two-way ANOVA based on
1502 the experimental design using GraphPad Prism Software. All values were expressed as the
1503 box-and-whisker plots or mean ± SD. Differences between two groups were analyzed using
1504 two-sided unpaired t-test with Welch's correction. Differences between multiple groups were
1505 analyzed using one- way or two-way ANOVA followed by Bonferroni post-hoc analysis.
1506 Differences were considered statistically significant for P values < 0.05.

1507

1508 **REFERENCES:**
1509

1510 Aits, S., Kricker, J., Liu, B., Ellegaard, A.M., Hamalisto, S., Tvingsholm, S., Corcelle-Termeau,
1511 E., Hogh, S., Farkas, T., Holm Jonassen, A., et al. (2015). Sensitive detection of lysosomal
1512 membrane permeabilization by lysosomal galectin puncta assay. Autophagy 11, 1408-1424.
1513 Alzheimer's Association (2020). 2020 Alzheimer's disease facts and figures. Alzheimers
1514 Dement.
1515 Amador-Ortiz, C., Lin, W.L., Ahmed, Z., Personett, D., Davies, P., Duara, R., Graff-Radford,
1516 N.R., Hutton, M.L., and Dickson, D.W. (2007). TDP-43 immunoreactivity in hippocampal
1517 sclerosis and Alzheimer's disease. Annals of neurology 61, 435-445.
1518 Anding, A.L., and Baehrecke, E.H. (2017). Cleaning House: Selective Autophagy of Organelles.
1519 Developmental cell 41, 10-22.
1520 Bettcher, B.M., Johnson, S.C., Fitch, R., Casaletto, K.B., Heffernan, K.S., Asthana, S.,
1521 Zetterberg, H., Blennow, K., Carlsson, C.M., Neuhaus, J., et al. (2018). Cerebrospinal Fluid and
1522 Plasma Levels of Inflammation Differentially Relate to CNS Markers of Alzheimer's Disease
1523 Pathology and Neuronal Damage. Journal of Alzheimer's disease : JAD 62, 385-397.
1524 Birnbaum, J.H., Wanner, D., Gietl, A.F., Saake, A., Kundig, T.M., Hock, C., Nitsch, R.M., and
1525 Tackenberg, C. (2018). Oxidative stress and altered mitochondrial protein expression in the
1526 absence of amyloid-beta and tau pathology in iPSC-derived neurons from sporadic Alzheimer's
1527 disease patients. Stem cell research 27, 121-130.
1528 Bourdenx, M., Daniel, J., Genin, E., Soria, F.N., Blanchard-Desce, M., Bezard, E., and Dehay,
1529 B. (2016). Nanoparticles restore lysosomal acidification defects: Implications for Parkinson and
1530 other lysosomal-related diseases. Autophagy 12, 472-483.
1531 Boza-Serrano, A., Ruiz, R., Sanchez-Varo, R., Garcia-Revilla, J., Yang, Y., Jimenez-Ferrer, I.,
1532 Paulus, A., Wennstrom, M., Vilalta, A., Allendorf, D., et al. (2019). Galectin-3, a novel
1533 endogenous TREM2 ligand, detrimentally regulates inflammatory response in Alzheimer's
1534 disease. Acta neuropathologica.
1535 Caiazzo, M., Dell'Anno, M.T., Dvoretskova, E., Lazarevic, D., Taverna, S., Leo, D., Sotnikova,
1536 T.D., Menegon, A., Roncaglia, P., Colciago, G., et al. (2011). Direct generation of functional
1537 dopaminergic neurons from mouse and human fibroblasts. Nature 476, 224-227.
1538 Cao, C., Prado, M.A., Sun, L., Rockowitz, S., Sliz, P., Paulo, J.A., Finley, D., and Fleming, M.D.
1539 (2021a). Maternal Iron Deficiency Modulates Placental Transcriptome and Proteome in Mid-
1540 Gestation of Mouse Pregnancy. The Journal of nutrition 151, 1073-1083.
1541 Cao, M., Luo, X., Wu, K., and He, X. (2021b). Targeting lysosomes in human disease: from
1542 basic research to clinical applications. Signal Transduct Target Ther 6, 379.
1543 Capano, L.S., Sato, C., Ficulle, E., Yu, A., Horie, K., Kwon, J.S., Burbach, K.F., Barthelemy,
1544 N.R., Fox, S.G., Karch, C.M., et al. (2022). Recapitulation of endogenous 4R tau expression
1545 and formation of insoluble tau in directly reprogrammed human neurons. Cell Stem Cell 29, 918-
1546 932 e918.
1547 Chakravorty, A., Jetto, C.T., and Manjithaya, R. (2019). Dysfunctional Mitochondria and
1548 Mitophagy as Drivers of Alzheimer's Disease Pathogenesis. Front Aging Neurosci 11, 311.
1549 Chen, J.J., Nathaniel, D.L., Raghavan, P., Nelson, M., Tian, R., Tse, E., Hong, J.Y., See, S.K.,
1550 Mok, S.A., Hein, M.Y., et al. (2019). Compromised function of the ESCRT pathway promotes

1551 endolysosomal escape of tau seeds and propagation of tau aggregation. The Journal of
1552 biological chemistry 294, 18952-18966.
1553 Chou, C.C., Zhang, Y., Umoh, M.E., Vaughan, S.W., Lorenzini, I., Liu, F., Sayegh, M., Donlin-
1554 Asp, P.G., Chen, Y.H., Duong, D.M., et al. (2018). TDP-43 pathology disrupts nuclear pore
1555 complexes and nucleocytoplasmic transport in ALS/FTD. Nature neuroscience 21, 228-239.
1556 Chung, C.Y., Shin, H.R., Berdan, C.A., Ford, B., Ward, C.C., Olzmann, J.A., Zoncu, R., and
1557 Nomura, D.K. (2019). Covalent targeting of the vacuolar H(+)-ATPase activates autophagy via
1558 mTORC1 inhibition. Nature chemical biology 15, 776-785.
1559 Cortes, C.J., and La Spada, A.R. (2019). TFEB dysregulation as a driver of autophagy
1560 dysfunction in neurodegenerative disease: Molecular mechanisms, cellular processes, and
1561 emerging therapeutic opportunities. Neurobiology of disease 122, 83-93.
1562 Craig, E.A. (2018). Hsp70 at the membrane: driving protein translocation. BMC Biol 16, 11.
1563 Cuervo, A.M., and Wong, E. (2014). Chaperone-mediated autophagy: roles in disease and
1564 aging. Cell Res 24, 92-104.
1565 DeTure, M.A., and Dickson, D.W. (2019). The neuropathological diagnosis of Alzheimer's
1566 disease. Molecular neurodegeneration 14, 32.
1567 Ditaranto, K., Tekirian, T.L., and Yang, A.J. (2001). Lysosomal membrane damage in soluble
1568 Abeta-mediated cell death in Alzheimer's disease. Neurobiology of disease 8, 19-31.
1569 Douglas, P.M., and Dillin, A. (2010). Protein homeostasis and aging in neurodegeneration. The
1570 Journal of cell biology 190, 719-729.
1571 Eapen, V.V., Swarup, S., Hoyer, M.J., Paulo, J.A., and Harper, J.W. (2021). Quantitative
1572 proteomics reveals the selectivity of ubiquitin-binding autophagy receptors in the turnover of
1573 damaged lysosomes by lysophagy. Elife 10.
1574 Eftekharzadeh, B., Daigle, J.G., Kapinos, L.E., Coyne, A., Schiantarelli, J., Carlomagno, Y.,
1575 Cook, C., Miller, S.J., Dujardin, S., Amaral, A.S., et al. (2018). Tau Protein Disrupts
1576 Nucleocytoplasmic Transport in Alzheimer's Disease. Neuron 99, 925-940.e927.
1577 Eng, J.K., Fischer, B., Grossmann, J., and Maccoss, M.J. (2008). A fast SEQUEST cross
1578 correlation algorithm. Journal of proteome research 7, 4598-4602.
1579 Eng, J.K., Jahan, T.A., and Hoopmann, M.R. (2013). Comet: an open-source MS/MS sequence
1580 database search tool. Proteomics 13, 22-24.
1581 Eng, J.K., McCormack, A.L., and Yates, J.R. (1994). An approach to correlate tandem mass
1582 spectral data of peptides with amino acid sequences in a protein database. J Am Soc Mass
1583 Spectrom 5, 976-989.
1584 Faizi, M., Bader, P.L., Saw, N., Nguyen, T.V., Beraki, S., Wyss-Coray, T., Longo, F.M., and
1585 Shamloo, M. (2012). Thy1-hAPP(Lond/Swe+) mouse model of Alzheimer's disease displays
1586 broad behavioral deficits in sensorimotor, cognitive and social function. Brain Behav 2, 142-154.
1587 Fruhmann, G., Marchal, C., Vignaud, H., Verduyckt, M., Talarek, N., De Virgilio, C., Winderickx,
1588 J., and Cullin, C. (2018). The Impact of ESCRT on Abeta1-42 Induced Membrane Lesions in a
1589 Yeast Model for Alzheimer's Disease. Frontiers in molecular neuroscience 11, 406.
1590 Galluzzi, L., Baehrecke, E.H., Ballabio, A., Boya, P., Bravo-San Pedro, J.M., Cecconi, F., Choi,
1591 A.M., Chu, C.T., Codogno, P., Colombo, M.I., et al. (2017). Molecular definitions of autophagy
1592 and related processes. The EMBO journal 36, 1811-1836.

1593 Gold, L., Ayers, D., Bertino, J., Bock, C., Bock, A., Brody, E.N., Carter, J., Dalby, A.B., Eaton,
1594 B.E., Fitzwater, T., et al. (2010). Aptamer-based multiplexed proteomic technology for biomarker
1595 discovery. PloS one 5, e15004.
1596 Gottschling, D.E., and Nyström, T. (2017). The Upsides and Downsides of Organelle
1597 Interconnectivity. Cell 169, 24-34.
1598 Gouras, G.K., Tsai, J., Naslund, J., Vincent, B., Edgar, M., Checler, F., Greenfield, J.P.,
1599 Haroutunian, V., Buxbaum, J.D., Xu, H., et al. (2000). Intraneuronal Abeta42 accumulation in
1600 human brain. The American journal of pathology 156, 15-20.
1601 Gowrishankar, S., Yuan, P., Wu, Y., Schrag, M., Paradise, S., Grutzendler, J., De Camilli, P.,
1602 and Ferguson, S.M. (2015). Massive accumulation of luminal protease-deficient axonal
1603 lysosomes at Alzheimer's disease amyloid plaques. Proceedings of the National Academy of
1604 Sciences of the United States of America 112, E3699-3708.
1605 Grubman, A., Chew, G., Ouyang, J.F., Sun, G., Choo, X.Y., McLean, C., Simmons, R.K.,
1606 Buckberry, S., Vargas-Landin, D.B., Poppe, D., et al. (2019). A single-cell atlas of entorhinal
1607 cortex from individuals with Alzheimer's disease reveals cell-type-specific gene expression
1608 regulation. Nature neuroscience 22, 2087-2097.
1609 Grubman, A., Choo, X.Y., Chew, G., Ouyang, J.F., Sun, G., Croft, N.P., Rossello, F.J.,
1610 Simmons, R., Buckberry, S., Landin, D.V., et al. (2021). Transcriptional signature in microglia
1611 associated with Abeta plaque phagocytosis. Nature communications 12, 3015.
1612 Hansson, J., Rafiee, M.R., Reiland, S., Polo, J.M., Gehring, J., Okawa, S., Huber, W.,
1613 Hochedlinger, K., and Krijgsveld, J. (2012). Highly coordinated proteome dynamics during
1614 reprogramming of somatic cells to pluripotency. Cell reports 2, 1579-1592.
1615 Harvey, R.J., Skelton-Robinson, M., and Rossor, M.N. (2003). The prevalence and causes of
1616 dementia in people under the age of 65 years. Journal of neurology, neurosurgery, and
1617 psychiatry 74, 1206-1209.
1618 Heneka, M.T., Kummer, M.P., Stutz, A., Delekate, A., Schwartz, S., Vieira-Saecker, A., Griep,
1619 A., Axt, D., Remus, A., Tzeng, T.C., et al. (2013). NLRP3 is activated in Alzheimer's disease
1620 and contributes to pathology in APP/PS1 mice. Nature 493, 674-678.
1621 Herdy, J.R., Traxler, L., Agarwal, R.K., Karbacher, L., Schlachetzki, J.C.M., Boehnke, L.,
1622 Zangwill, D., Galasko, D., Glass, C.K., Mertens, J., et al. (2022). Increased post-mitotic
1623 senescence in aged human neurons is a pathological feature of Alzheimer's disease. Cell Stem
1624 Cell 29, 1637-1652.e1636.
1625 Hipp, M.S., Park, S.H., and Hartl, F.U. (2014). Proteostasis impairment in protein-misfolding and
1626 -aggregation diseases. Trends Cell Biol 24, 506-514.
1627 Hondius, D.C., Koopmans, F., Leistner, C., Pita-Illobre, D., Peferoen-Baert, R.M., Marbus, F.,
1628 Paliukhovich, I., Li, K.W., Rozemuller, A.J.M., Hoozemans, J.J.M., et al. (2021). The proteome
1629 of granulovacuolar degeneration and neurofibrillary tangles in Alzheimer's disease. Acta
1630 neuropathologica 141, 341-358.
1631 Hughes, A.L., and Gottschling, D.E. (2012). An early age increase in vacuolar pH limits
1632 mitochondrial function and lifespan in yeast. Nature 492, 261-265.
1633 Huh, C.J., Zhang, B., Victor, M.B., Dahiya, S., Batista, L.F., Horvath, S., and Yoo, A.S. (2016).
1634 Maintenance of age in human neurons generated by microRNA-based neuronal conversion of
1635 fibroblasts. Elife 5.

1636 Hung, C.O.Y., and Livesey, F.J. (2018). Altered gamma-Secretase Processing of APP Disrupts
1637 Lysosome and Autophagosome Function in Monogenic Alzheimer's Disease. Cell reports 25,
1638 3647-3660 e3642.
1639 Huttlin, E.L., Jedrychowski, M.P., Elias, J.E., Goswami, T., Rad, R., Beausoleil, S.A., Villén, J.,
1640 Haas, W., Sowa, M.E., and Gygi, S.P. (2010). A tissue-specific atlas of mouse protein
1641 phosphorylation and expression. Cell 143, 1174-1189.
1642 Israel, M.A., Yuan, S.H., Bardy, C., Reyna, S.M., Mu, Y., Herrera, C., Hefferan, M.P., Van Gorp,
1643 S., Nazor, K.L., Boscolo, F.S., et al. (2012). Probing sporadic and familial Alzheimer's disease
1644 using induced pluripotent stem cells. Nature 482, 216-220.
1645 Jiang, P., Gan, M., Yen, S.H., McLean, P.J., and Dickson, D.W. (2017). Impaired endo-
1646 lysosomal membrane integrity accelerates the seeding progression of alpha-synuclein
1647 aggregates. Scientific reports 7, 7690.
1648 Jimenez, A.J., Maiuri, P., Lafaurie-Janvore, J., Divoux, S., Piel, M., and Perez, F. (2014).
1649 ESCRT machinery is required for plasma membrane repair. Science (New York, NY) 343,
1650 1247136.
1651 Josephs, K.A., Murray, M.E., Whitwell, J.L., Parisi, J.E., Petrucelli, L., Jack, C.R., Petersen,
1652 R.C., and Dickson, D.W. (2014). Staging TDP-43 pathology in Alzheimer's disease. Acta
1653 neuropathologica 127, 441-450.
1654 Kaushik, S., and Cuervo, A.M. (2015). Proteostasis and aging. Nature medicine 21, 1406-1415.
1655 Kim, C.H., Tworoger, S.S., Stampfer, M.J., Dillon, S.T., Gu, X., Sawyer, S.J., Chan, A.T.,
1656 Libermann, T.A., and Eliassen, A.H. (2018a). Stability and reproducibility of proteomic profiles
1657 measured with an aptamer-based platform. Scientific reports 8, 8382.
1658 Kim, Y., Zheng, X., Ansari, Z., Bunnell, M.C., Herdy, J.R., Traxler, L., Lee, H., Paquola, A.C.M.,
1659 Blithikioti, C., Ku, M., et al. (2018b). Mitochondrial Aging Defects Emerge in Directly
1660 Reprogrammed Human Neurons due to Their Metabolic Profile. Cell reports 23, 2550-2558.
1661 Kirkegaard, T., Roth, A.G., Petersen, N.H., Mahalka, A.K., Olsen, O.D., Moilanen, I., Zylicz, A.,
1662 Knudsen, J., Sandhoff, K., Arenz, C., et al. (2010). Hsp70 stabilizes lysosomes and reverts
1663 Niemann-Pick disease-associated lysosomal pathology. Nature 463, 549-553.
1664 Köhler, C. (2016). Granulovacuolar degeneration: a neurodegenerative change that
1665 accompanies tau pathology. Acta neuropathologica 132, 339-359.
1666 Kravić, B., Bionda, T., Siebert, A., Gahlot, P., Levantovsky, S., Behrends, C., and Meyer, H.
1667 (2022). Ubiquitin profiling of lysophagy identifies actin stabilizer CNN2 as a target of VCP/p97
1668 and uncovers a link to HSPB1. Molecular cell 82, 2633-2649.e2637.
1669 Kwart, D., Gregg, A., Scheckel, C., Murphy, E.A., Paquet, D., Duffield, M., Fak, J., Olsen, O.,
1670 Darnell, R.B., and Tessier-Lavigne, M. (2019). A Large Panel of Isogenic APP and PSEN1
1671 Mutant Human iPSC Neurons Reveals Shared Endosomal Abnormalities Mediated by APP β-
1672 CTFs, Not Aβ. Neuron 104, 256-270.e255.
1673 Labbadia, J., and Morimoto, R.I. (2015). The biology of proteostasis in aging and disease.
1674 Annual review of biochemistry 84, 435-464.
1675 Lackie, R.E., Maciejewski, A., Ostapchenko, V.G., Marques-Lopes, J., Choy, W.Y., Duennwald,
1676 M.L., Prado, V.F., and Prado, M.A.M. (2017). The Hsp70/Hsp90 Chaperone Machinery in
1677 Neurodegenerative Diseases. Frontiers in neuroscience 11, 254.
1678 Lagomarsino, V.N., Pearse, R.V., 2nd, Liu, L., Hsieh, Y.C., Fernandez, M.A., Vinton, E.A., Paull,
1679 D., Felsky, D., Tasaki, S., Gaiteri, C., et al. (2021). Stem cell-derived neurons reflect features of

1680 protein networks, neuropathology, and cognitive outcome of their aged human donors. Neuron
1681 109, 3402-3420.e3409.
1682 Laskowska, E., Kuczynska-Wisnik, D., and Lipinska, B. (2019). Proteomic analysis of protein
1683 homeostasis and aggregation. J Proteomics 198, 98-112.
1684 Lee, J.H., McBrayer, M.K., Wolfe, D.M., Haslett, L.J., Kumar, A., Sato, Y., Lie, P.P., Mohan, P.,
1685 Coffey, E.E., Kompella, U., et al. (2015). Presenilin 1 Maintains Lysosomal Ca(2+) Homeostasis
1686 via TRPML1 by Regulating vATPase-Mediated Lysosome Acidification. Cell reports 12, 1430-
1687 1444.
1688 Lee, J.H., Yang, D.S., Goulbourne, C.N., Im, E., Stavrides, P., Pensalfini, A., Chan, H.,
1689 Bouchet-Marquis, C., Bleiwas, C., Berg, M.J., et al. (2022). Faulty autolysosome acidification in
1690 Alzheimer's disease mouse models induces autophagic build-up of Aβ in neurons, yielding
1691 senile plaques. Nature neuroscience 25, 688-701.
1692 Lee, J.H., Yu, W.H., Kumar, A., Lee, S., Mohan, P.S., Peterhoff, C.M., Wolfe, D.M., Martinez-
1693 Vicente, M., Massey, A.C., Sovak, G., et al. (2010). Lysosomal proteolysis and autophagy
1694 require presenilin 1 and are disrupted by Alzheimer-related PS1 mutations. Cell 141, 1146-
1695 1158.
1696 Liu, X., Li, J., Gygi, S.P., and Paulo, J.A. (2022). Profiling Yeast Deletion Strains Using Sample
1697 Multiplexing and Network-Based Analyses. Journal of proteome research 21, 1525-1536.
1698 Logan, T., Simon, M.J., Rana, A., Cherf, G.M., Srivastava, A., Davis, S.S., Low, R.L.Y., Chiu,
1699 C.L., Fang, M., Huang, F., et al. (2021). Rescue of a lysosomal storage disorder caused by Grn
1700 loss of function with a brain penetrant progranulin biologic. Cell 184, 4651-4668 e4625.
1701 Maejima, I., Takahashi, A., Omori, H., Kimura, T., Takabatake, Y., Saitoh, T., Yamamoto, A.,
1702 Hamasaki, M., Noda, T., Isaka, Y., et al. (2013). Autophagy sequesters damaged lysosomes to
1703 control lysosomal biogenesis and kidney injury. The EMBO journal 32, 2336-2347.
1704 Mahmoudi, S., and Brunet, A. (2012). Aging and reprogramming: a two-way street. Current
1705 opinion in cell biology 24, 744-756.
1706 Mansuroglu, Z., Benhelli-Mokrani, H., Marcato, V., Sultan, A., Violet, M., Chauderlier, A.,
1707 Delattre, L., Loyens, A., Talahari, S., Begard, S., et al. (2016). Loss of Tau protein affects the
1708 structure, transcription and repair of neuronal pericentromeric heterochromatin. Scientific
1709 reports 6, 33047.
1710 Masters, C.L., Multhaup, G., Simms, G., Pottgiesser, J., Martins, R.N., and Beyreuther, K.
1711 (1985). Neuronal origin of a cerebral amyloid: neurofibrillary tangles of Alzheimer's disease
1712 contain the same protein as the amyloid of plaque cores and blood vessels. The EMBO journal
1713 4, 2757-2763.
1714 Mathys, H., Davila-Velderrain, J., Peng, Z., Gao, F., Mohammadi, S., Young, J.Z., Menon, M.,
1715 He, L., Abdurrob, F., Jiang, X., et al. (2019). Single-cell transcriptomic analysis of Alzheimer's
1716 disease. Nature 570, 332-337.
1717 McAlister, G.C., Nusinow, D.P., Jedrychowski, M.P., Wühr, M., Huttlin, E.L., Erickson, B.K.,
1718 Rad, R., Haas, W., and Gygi, S.P. (2014). MultiNotch MS3 enables accurate, sensitive, and
1719 multiplexed detection of differential expression across cancer cell line proteomes. Analytical
1720 chemistry 86, 7150-7158.
1721 Mertens, J., Herdy, J.R., Traxler, L., Schafer, S.T., Schlachetzki, J.C.M., Böhnke, L., Reid, D.A.,
1722 Lee, H., Zangwill, D., Fernandes, D.P., et al. (2021). Age-dependent instability of mature

1723 neuronal fate in induced neurons from Alzheimer's patients. Cell Stem Cell 28, 1533-
1724 1548.e1536.
1725 Mertens, J., Paquola, A.C., Ku, M., Hatch, E., Bohnke, L., Ladjevardi, S., McGrath, S.,
1726 Campbell, B., Lee, H., Herdy, J.R., et al. (2015). Directly Reprogrammed Human Neurons
1727 Retain Aging-Associated Transcriptomic Signatures and Reveal Age-Related
1728 Nucleocytoplasmic Defects. Cell Stem Cell 17, 705-718.
1729 Miller, J.D., Ganat, Y.M., Kishinevsky, S., Bowman, R.L., Liu, B., Tu, E.Y., Mandal, P.K., Vera,
1730 E., Shim, J.W., Kriks, S., et al. (2013). Human iPSC-based modeling of late-onset disease via
1731 progerin-induced aging. Cell Stem Cell 13, 691-705.
1732 Mochizuki, A., Tamaoka, A., Shimohata, A., Komatsuzaki, Y., and Shoji, S. (2000). Abeta42-
1733 positive non-pyramidal neurons around amyloid plaques in Alzheimer's disease. Lancet 355, 42-
1734 43.
1735 Moreau, D., Vacca, F., Vossio, S., Scott, C., Colaco, A., Paz Montoya, J., Ferguson, C.,
1736 Damme, M., Moniatte, M., Parton, R.G., et al. (2019). Drug-induced increase in
1737 lysobisphosphatidic acid reduces the cholesterol overload in Niemann-Pick type C cells and
1738 mice. EMBO reports 20, e47055.
1739 Mulay, S.R., and Anders, H.J. (2017). Crystal nephropathies: mechanisms of crystal-induced
1740 kidney injury. Nat Rev Nephrol 13, 226-240.
1741 Nativio, R., Donahue, G., Berson, A., Lan, Y., Amlie-Wolf, A., Tuzer, F., Toledo, J.B., Gosai,
1742 S.J., Gregory, B.D., Torres, C., et al. (2018). Dysregulation of the epigenetic landscape of
1743 normal aging in Alzheimer's disease. Nature neuroscience 21, 497-505.
1744 Nguyen, A.T., Prado, M.A., Schmidt, P.J., Sendamarai, A.K., Wilson-Grady, J.T., Min, M.,
1745 Campagna, D.R., Tian, G., Shi, Y., Dederer, V., et al. (2017). UBE2O remodels the proteome
1746 during terminal erythroid differentiation. Science (New York, NY) 357.
1747 Nijholt, D.A., de Graaf, T.R., van Haastert, E.S., Oliveira, A.O., Berkers, C.R., Zwart, R., Ovaa,
1748 H., Baas, F., Hoozemans, J.J., and Scheper, W. (2011). Endoplasmic reticulum stress activates
1749 autophagy but not the proteasome in neuronal cells: implications for Alzheimer's disease. Cell
1750 death and differentiation 18, 1071-1081.
1751 Nixon, R.A., and Yang, D.S. (2011). Autophagy failure in Alzheimer's disease--locating the
1752 primary defect. Neurobiology of disease 43, 38-45.
1753 Nixon, R.A., Yang, D.S., and Lee, J.H. (2008). Neurodegenerative lysosomal disorders: a
1754 continuum from development to late age. Autophagy 4, 590-599.
1755 Pang, Z.P., Yang, N., Vierbuchen, T., Ostermeier, A., Fuentes, D.R., Yang, T.Q., Citri, A.,
1756 Sebastiano, V., Marro, S., Sudhof, T.C., et al. (2011). Induction of human neuronal cells by
1757 defined transcription factors. Nature 476, 220-223.
1758 Petkovic, M., O'Brien, C.E., and Jan, Y.N. (2021). Interorganelle communication, aging, and
1759 neurodegeneration. Genes Dev 35, 449-469.
1760 Piras, A., Collin, L., Grüninger, F., Graff, C., and Rönnbäck, A. (2016). Autophagic and
1761 lysosomal defects in human tauopathies: analysis of post-mortem brain from patients with
1762 familial Alzheimer disease, corticobasal degeneration and progressive supranuclear palsy. Acta
1763 Neuropathol Commun 4, 22.
1764 Pohl, C., and Dikic, I. (2019). Cellular quality control by the ubiquitin-proteasome system and
1765 autophagy. Science (New York, NY) 366, 818-822.

1766 Qiu, C., Kivipelto, M., and von Strauss, E. (2009). Epidemiology of Alzheimer's disease:
1767 occurrence, determinants, and strategies toward intervention. Dialogues in clinical neuroscience
1768 11, 111-128.
1769 Radulovic, M., Schink, K.O., Wenzel, E.M., Nahse, V., Bongiovanni, A., Lafont, F., and
1770 Stenmark, H. (2018). ESCRT-mediated lysosome repair precedes lysophagy and promotes cell
1771 survival. The EMBO journal.
1772 Raj, T., Li, Y.I., Wong, G., Humphrey, J., Wang, M., Ramdhani, S., Wang, Y.C., Ng, B., Gupta,
1773 I., Haroutunian, V., et al. (2018). Integrative transcriptome analyses of the aging brain implicate
1774 altered splicing in Alzheimer's disease susceptibility. Nature genetics 50, 1584-1592.
1775 Rappsilber, J., Ishihama, Y., and Mann, M. (2003). Stop and go extraction tips for matrix-
1776 assisted laser desorption/ionization, nanoelectrospray, and LC/MS sample pretreatment in
1777 proteomics. Analytical chemistry 75, 663-670.
1778 Rentzos, M., Zoga, M., Paraskevas, G.P., Kapaki, E., Rombos, A., Nikolaou, C., Tsoutsou, A.,
1779 and Vassilopoulos, D. (2006). IL-15 is elevated in cerebrospinal fluid of patients with
1780 Alzheimer's disease and frontotemporal dementia. Journal of geriatric psychiatry and neurology
1781 19, 114-117.
1782 Riku, Y., Duyckaerts, C., Boluda, S., Plu, I., Le Ber, I., Millecamps, S., Salachas, F., Brainbank
1783 Neuro, C.E.B.N.N., Yoshida, M., Ando, T., et al. (2019). Increased prevalence of
1784 granulovacuolar degeneration in C9orf72 mutation. Acta neuropathologica 138, 783-793.
1785 Rockenstein, E., Mallory, M., Mante, M., Sisk, A., and Masliaha, E. (2001). Early formation of
1786 mature amyloid-beta protein deposits in a mutant APP transgenic model depends on levels of
1787 Abeta(1-42). Journal of neuroscience research 66, 573-582.
1788 Salminen, A., Kaarniranta, K., Haapasalo, A., Hiltunen, M., Soininen, H., and Alafuzoff, I.
1789 (2012). Emerging role of p62/sequestosome-1 in the pathogenesis of Alzheimer's disease.
1790 Progress in neurobiology 96, 87-95.
1791 Scheffer, L.L., Sreetama, S.C., Sharma, N., Medikayala, S., Brown, K.J., Defour, A., and
1792 Jaiswal, J.K. (2014). Mechanism of Ca(2)(+)-triggered ESCRT assembly and regulation of cell
1793 membrane repair. Nature communications 5, 5646.
1794 Schweppe, D.K., Eng, J.K., Yu, Q., Bailey, D., Rad, R., Navarrete-Perea, J., Huttlin, E.L.,
1795 Erickson, B.K., Paulo, J.A., and Gygi, S.P. (2020a). Full-Featured, Real-Time Database
1796 Searching Platform Enables Fast and Accurate Multiplexed Quantitative Proteomics. Journal of
1797 proteome research 19, 2026-2034.
1798 Schweppe, D.K., Prasad, S., Belford, M.W., Navarrete-Perea, J., Bailey, D.J., Huguet, R.,
1799 Jedrychowski, M.P., Rad, R., McAlister, G., Abbatiello, S.E., et al. (2019). Characterization and
1800 Optimization of Multiplexed Quantitative Analyses Using High-Field Asymmetric-Waveform Ion
1801 Mobility Mass Spectrometry. Analytical chemistry 91, 4010-4016.
1802 Schweppe, D.K., Rusin, S.F., Gygi, S.P., and Paulo, J.A. (2020b). Optimized Workflow for
1803 Multiplexed Phosphorylation Analysis of TMT-Labeled Peptides Using High-Field Asymmetric
1804 Waveform Ion Mobility Spectrometry. Journal of proteome research 19, 554-560.
1805 Settembre, C., Di Malta, C., Polito, V.A., Garcia Arencibia, M., Vetrini, F., Erdin, S., Erdin, S.U.,
1806 Huynh, T., Medina, D., Colella, P., et al. (2011). TFEB links autophagy to lysosomal biogenesis.
1807 Science (New York, NY) 332, 1429-1433.
1808 Skowyra, M.L., Schlesinger, P.H., Naismith, T.V., and Hanson, P.I. (2018). Triggered
1809 recruitment of ESCRT machinery promotes endolysosomal repair. Science (New York, NY) 360.

1810 Studer, L., Vera, E., and Cornacchia, D. (2015). Programming and Reprogramming Cellular Age
1811 in the Era of Induced Pluripotency. Cell Stem Cell 16, 591-600.
1812 Su, J.H., Kesslak, JP., Head, E., and Cotman, C.W.(2002) Caspase-cleaved amyloid precursor
1813 protein and activated caspase-3 are co-localized in the granules of granulovacuolar
1814 degeneration in Alzheimer's disease and Down's syndrome brain. Acta neuropathologica104,1-
1815 6.
1816 Talboom, J.S., Velazquez, R., and Oddo, S. (2015). The mammalian target of rapamycin at the
1817 crossroad between cognitive aging and Alzheimer's disease. NPJ Aging Mech Dis 1, 15008.
1818 Tan, J.X., and Finkel, T. (2022). A phosphoinositide signalling pathway mediates rapid
1819 lysosomal repair. Nature 609, 815-821.
1820 Tanabe, K., Ang, C.E., Chanda, S., Olmos, V.H., Haag, D., Levinson, D.F., Sudhof, T.C., and
1821 Wernig, M. (2018). Transdifferentiation of human adult peripheral blood T cells into neurons.
1822 Proceedings of the National Academy of Sciences of the United States of America.
1823 Tang, Y., Liu, M.L., Zang, T., and Zhang, C.L. (2017). Direct Reprogramming Rather than iPSC-
1824 Based Reprogramming Maintains Aging Hallmarks in Human Motor Neurons. Frontiers in
1825 molecular neuroscience 10, 359.
1826 Tian, R., Abarientos, A., Hong, J., Hashemi, S.H., Yan, R., Dräger, N., Leng, K., Nalls, M.A.,
1827 Singleton, A.B., Xu, K., et al. (2021). Genome-wide CRISPRi/a screens in human neurons link
1828 lysosomal failure to ferroptosis. Nature neuroscience 24, 1020-1034.
1829 Tong, B.C., Wu, A.J., Li, M., and Cheung, K.H. (2018). Calcium signaling in Alzheimer's disease
1830 & therapies. Biochim Biophys Acta Mol Cell Res 1865, 1745-1760.
1831 Traxler, L., Herdy, J.R., Stefanoni, D., Eichhorner, S., Pelucchi, S., Szücs, A., Santagostino, A.,
1832 Kim, Y., Agarwal, R.K., Schlachetzki, J.C.M., et al. (2022). Warburg-like metabolic
1833 transformation underlies neuronal degeneration in sporadic Alzheimer's disease. Cell
1834 metabolism 34, 1248-1263.e1246.
1835 Vest, R.T., Chou, C.C., Zhang, H., Haney, M.S., Li, L., Laqtom, N.N., Chang, B., Shuken, S.,
1836 Nguyen, A., Yerra, L., et al. (2022). Small molecule C381 targets the lysosome to reduce
1837 inflammation and ameliorate disease in models of neurodegeneration. Proceedings of the
1838 National Academy of Sciences of the United States of America 119, e2121609119.
1839 Victor, M.B., Richner, M., Olsen, H.E., Lee, S.W., Monteys, A.M., Ma, C., Huh, C.J., Zhang, B.,
1840 Davidson, B.L., Yang, X.W., et al. (2018). Striatal neurons directly converted from Huntington's
1841 disease patient fibroblasts recapitulate age-associated disease phenotypes. Nature
1842 neuroscience 21, 341-352.
1843 Vierbuchen, T., Ostermeier, A., Pang, Z.P., Kokubu, Y., Sudhof, T.C., and Wernig, M. (2010).
1844 Direct conversion of fibroblasts to functional neurons by defined factors. Nature 463, 1035-1041.
1845 Villeda, S.A., Plambeck, K.E., Middeldorp, J., Castellano, J.M., Mosher, K.I., Luo, J., Smith,
1846 L.K., Bieri, G., Lin, K., Berdnik, D., et al. (2014). Young blood reverses age-related impairments
1847 in cognitive function and synaptic plasticity in mice. Nature medicine 20, 659-663.
1848 Vizcaíno, J.A., Deutsch, E.W., Wang, R., Csordas, A., Reisinger, F., Ríos, D., Dianes, J.A., Sun,
1849 Z., Farrah, T., Bandeira, N., et al. (2014). ProteomeXchange provides globally coordinated
1850 proteomics data submission and dissemination. Nature biotechnology 32, 223-226.
1851 Wang, D., Zhang, J., Jiang, W., Cao, Z., Zhao, F., Cai, T., Aschner, M., and Luo, W. (2017). The
1852 role of NLRP3-CASP1 in inflammasome-mediated neuroinflammation and autophagy

dysfunction in manganese-induced, hippocampal-dependent impairment of learning and memory ability. Autophagy 13, 914-927.
Wang, Z., Wang, Q., Li, S., Li, X.J., Yang, W., and He, D. (2022). Microglial autophagy in Alzheimer's disease and Parkinson's disease. Front Aging Neurosci 14, 1065183.
Whyte, L.S., Lau, A.A., Hemsley, K.M., Hopwood, J.J., and Sargeant, T.J. (2017). Endo-lysosomal and autophagic dysfunction: a driving factor in Alzheimer's disease? Journal of neurochemistry 140, 703-717.
Wiersma, V.I., van Ziel, A.M., Vazquez-Sanchez, S., Nolle, A., Berenjeno-Correa, E., Bonaterra-Pastra, A., Clavaguera, F., Tolnay, M., Musters, R.J.P., van Weering, J.R.T., et al. (2019). Granulovacuolar degeneration bodies are neuron-selective lysosomal structures induced by intracellular tau pathology. Acta neuropathologica 138, 943-970.
Willén, K., Edgar, J.R., Hasegawa, T., Tanaka, N., Futter, C.E., and Gouras, G.K. (2017). Aβ accumulation causes MVB enlargement and is modelled by dominant negative VPS4A. Molecular neurodegeneration 12, 61.
Wolfe, D.M., Lee, J.H., Kumar, A., Lee, S., Orenstein, S.J., and Nixon, R.A. (2013). Autophagy failure in Alzheimer's disease and the role of defective lysosomal acidification. Eur J Neurosci 37, 1949-1961.
Yamoah, A., Tripathi, P., Sechi, A., Kohler, C., Guo, H., Chandrasekar, A., Nolte, K.W., Wruck, C.J., Katona, I., Anink, J., et al. (2020). Aggregates of RNA Binding Proteins and ER Chaperones Linked to Exosomes in Granulovacuolar Degeneration of the Alzheimer's Disease Brain. Journal of Alzheimer's disease : JAD 75, 139-156.
Yoon, L., Botham, R.C., Verhelle, A., Sanz-Martinez, P., Xu, J., Cole, C.M., Tan, E.P., Chou, C.-C., Cuoco, C.A., Massey, L.A., et al. (2022). mTOR inhibitor-independent Autophagy Activator Ameliorates Tauopathy and Prionopathy Neurodegeneration Phenotypes. bioRxiv, 2022.2009.2029.509997.
Zhang, M.J., Pisco, A.O., Darmanis, S., and Zou, J. (2021). Mouse aging cell atlas analysis reveals global and cell type-specific aging signatures. Elife 10.
Zhang, W., Xu, C., Sun, J., Shen, H.M., Wang, J., and Yang, C. (2022). Impairment of the autophagy-lysosomal pathway in Alzheimer's diseases: Pathogenic mechanisms and therapeutic potential. Acta Pharm Sin B 12, 1019-1040.
Zhao, J., Fu, Y., Yamazaki, Y., Ren, Y., Davis, M.D., Liu, C.C., Lu, W., Wang, X., Chen, K., Cherukuri, Y., et al. (2020). APOE4 exacerbates synapse loss and neurodegeneration in Alzheimer's disease patient iPSC-derived cerebral organoids. Nature communications 11, 5540.